Review Article

Stephan Gräf*

Formation of laser-induced periodic surface structures on different materials: fundamentals, properties and applications

https://doi.org/10.1515/aot-2019-0062
Received November 22, 2019; accepted February 26, 2020; previously published online April 17, 2020

Abstract: The use of ultra-short pulsed lasers enables the fabrication of laser-induced periodic surface structures (LIPSS) on various materials following a single-step, direct-writing technique. These specific, well-ordered nanostructures with periodicities in the order of the utilised laser wavelength facilitate the engineering of surfaces with functional properties. This review paper discusses the physical background of LIPSS formation on substrates with different material properties. Using the examples of structural colours, specific wetting states and the reduction of friction and wear, this work presents experimental approaches that allow to deliberately influence the LIPSS formation process and thus tailor the surface properties. Finally, the review concludes with some future developments and perspectives related to forthcoming applications of LIPSS-based surfaces are discussed.

Keywords: functional surfaces; laser-induced periodic surface structures; nanostructuring; selective surface structuring; ultra-short pulsed lasers.

1 Introduction

The irradiation of a material surface with linearly polarised, ultra-short pulsed laser radiation allows the generation of specific, well-ordered nanostructures with periodicities Λ in the order of the utilised laser wavelength λ. These so-called laser-induced periodic surface structures (LIPSS) were the subject of numerous studies in the past, demonstrating the great potential of LIPSS to engineer surfaces with versatile functional properties [1–4]. The generation of LIPSS was demonstrated on almost all types of materials, including metals, semiconductors and dielectrics [5]. In the case of composites, the deviating absorption of the fs-laser radiation by the components allows a selective surface structuring with LIPSS [6–8]. LIPSS can be characterised as a modulation of the surface topography on the micro- and nanoscale, which results from the irradiation with linearly polarised laser radiation close to the ablation threshold. They can be easily produced in a single-step direct-writing technique without the need for chemicals or expensive vacuum-based processes. Furthermore, they can be applied from a microscopic scale, i.e. limited to the focal spot area of the processing beam, to a macroscopic scale, i.e. homogenously on large surface areas (cm^2-m^2). Furthermore, the numerous influencing parameters – both in terms of the material properties and the laser process – allow the tailored adjustment of the LIPSS properties (e.g. periodicity and alignment of the structures, chemical composition, etc.) to the respective application.

The present work summarises the formation of LIPSS on different types of substrates with different material properties and discusses potential applications, such as variable structural colours, specific wetting states and the tribological properties of composites. The studies are based on a systematic surface characterisation concerning their topography by optical microscopy (OM), scanning electron microscopy (SEM), atomic force microscopy (AFM) and white-light interference microscopy (WLIM). The chemical and structural composition of the material surface upon fs-laser irradiation was analysed amongst others by Raman spectroscopy, X-ray photoelectron spectroscopy (XPS), Fourier-transform infrared spectroscopy (FTIR) and energy-dispersive X-ray spectroscopy (EDX). The wettability of the surfaces was studied with respect to global and local contact angles based on the sessile drop method and confocal laser scanning microscopy (CLSM).

***Corresponding author: Stephan Gräf,** Otto Schott Institute of Materials Research (OSIM), Friedrich Schiller University Jena, Löbdergraben 32, 07743 Jena, Germany,
e-mail: stephan.graef@uni-jena.de. https://orcid.org/0000-0003-2849-1377

2 Formation and properties of laser-induced periodic surface structures

LIPSS are nanostructures that are created in the form of a modulated surface topography in the focal spot of the fs-laser beam. As shown in Figure 1, using fused silica as an example, LIPSS are classified according to their spatial period Λ into low-spatial frequency LIPSS (LSFL) and high-spatial frequency LIPSS (HSFL). LSFL are characterised by $\Lambda \sim \lambda$ for strong absorbing materials (metals, semiconductors) and $\Lambda \sim \lambda/n$ for dielectrics, where n refers to the refractive index of the dielectric material [5, 9, 10].

The orientation of the structures with respect to the linear beam polarisation depends on the type of material and its dielectric function [1]. On metals and semiconductors, LSFL are predominantly aligned perpendicular to the electrical field (E-field) vector [5]. Some dielectric materials (e.g. fused silica) and certain polymers show LSFL with an orientation that is parallel to the laser beam polarisation [5, 9–11]. The rapid development of ultra-short pulsed lasers over the past decades has contributed to HSFL becoming an increasingly important area of research, as these structures with periods much smaller than λ have been predominantly observed for irradiation with ps- and fs-laser pulses. They have been demonstrated mainly on transparent materials but also on metals with an orientation either parallel or perpendicular to the E-field vector, depending on the material [5].

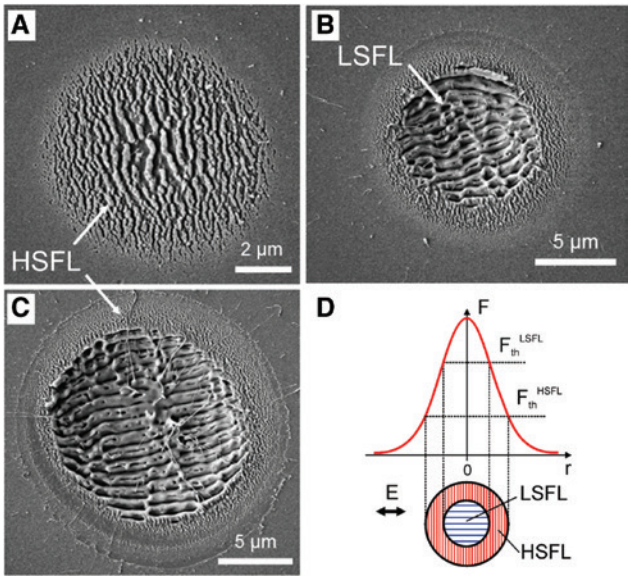

Figure 1: The SEM micrographs of fused silica surfaces after fs-laser irradiation with $N = 5$ pulses ($\lambda = 1025$ nm, $\tau_{imp} = 300$ fs) showing (A) HSFL and (B, C) LSFL. The assignment of both LIPSS types to the fluence distribution of the Gaussian laser radiation in the focal spot and to the respective threshold fluences F_{th} is illustrated in (D) [9, 10].

The observed periodicity of LSFL in the order of λ and the influence of the beam polarisation on their orientation suggest an electromagnetic origin. Emmony proposed the formation of LSFL by the interaction of the incident laser radiation with surface electromagnetic waves generated at surface defects and scratches [12]. This basic idea was later extended, e.g. by the consideration of surface plasmon polaritons (SPPs) [13–17]. Plasmonic theory describes the formation of LSFL based on the interference of SPPs with the incident laser radiation, which results in a spatially modulated energy deposition at the material surface [17]. In this context, a key aspect is related to the surface roughness, which is required for the excitation of SPPs on flat substrate surfaces [14, 18]. A major contribution to the field is provided by Sipe theory, which is still one of the most widely accepted theories on LIPSS formation [14]. The theory is based on the interference of the incident laser radiation with surface electromagnetic waves, which are generated by scattering at the rough surface. Using the materials optical properties as input data, Sipe theory allows the calculation of the LIPSS properties (spatial periods, orientation with respect to polarisation) depending on the angle of incidence, polarisation direction and wavelength of the incident laser radiation. As a result, the so-called efficacy factor, $\eta(\boldsymbol{k})$, can be calculated as a measure for the efficacy of a rough surface to absorb energy at the wave vector $\boldsymbol{k}$. The limitations of the model are related to the presumption of a homogenous dielectric permittivity of the material and an irradiation in vacuum. Moreover, feedback phenomena, e.g. upon multi-pulse irradiation, are not considered and some types of LIPSS, such as HSFL, are not properly described. Feedback processes can occur between successive pulses (inter-pulse effects), but also already during a single pulse (intra-pulse effects) [1]. The latter is given, for example, by the transient modification of the optical properties as a function of time and of space in laser-irradiated band gap materials due to the transient excitation of electrons into the conduction band [19]. This aspect was considered by Bonse et al. by combining Sipe theory with the Drude model [20, 21]. The Drude model provides the dielectric function ε^* of the laser-excited material by adding the additional Drude term $\Delta\varepsilon$ to the complex dielectric function $\varepsilon = \varepsilon_r + i\varepsilon_i = (n + ik)^2$ of the non-excited material [22]

$$\varepsilon^* = \varepsilon + \Delta\varepsilon = \varepsilon - \frac{e^2 N_e}{\varepsilon_0 m_{opt} m_e \omega^2 \left(1 + \frac{i}{\omega\tau_D}\right)},$$

where e represents the electron charge, N_e is the laser-induced electron density, m_e is the electron mass, ε_0 is the vacuum dielectric permittivity and ω is the laser angular frequency.

An alternative approach to explain LSFL formation is provided by the self-organisation of the irradiated material. Here, the structure formation is described based on processes occurring during the relaxation of the surface from a laser-induced state of thermodynamic instability. Therefore, the longer-term post-irradiation aspects are considered. A central point in this framework is given by hydrodynamics, which is triggered by, for example, the Marangoni effect due to temperature gradients [23, 24], recoil forces induced by evaporation [25, 26], hydrodynamic instabilities [27, 28], as well as material reorganisation driven by erosion and diffusion [29, 30]. Some of these studies consider the electromagnetic origin and its resulting inhomogeneous energy deposition as a seed for the subsequent hydrodynamic processes by considering a spatially modulated electron temperature along the material surface [24–26].

The formation of HSFL is still controversially discussed in the literature and a deep understanding of the formation mechanism is missing. Most of the models also consider electromagnetic origins, including the intrapulse alteration of the optical properties [31], non-linear Kerr effect [22], superficial oxidation on metals [32, 33], surface second harmonic generation [21, 34], plasmonic effects [35] and SPP excitation [36]. Rudenko et al. recently revealed that HSFL formation on fused silica is driven by the interference between the incident laser field and the scattered near-field below the surface, which requires the presence of initial inhomogeneities, electron defects or scattering centres [37]. Analogous to LSFL, the framework of self-organisation has been used to describe HSFL formation [29].

From the perspective of applications, LIPSS structuring primarily leads to a modification of the surface topography, which is required to realise the desired functional features of the material surface (see Ch. 3). However, the available experimental studies reveal that the chemical modification of the surface (in the form of, for example, oxidation, contamination and amorphisation) plays an equally important role as the achieved surface properties cannot be explained solely by topographical aspects [7, 8, 38–41]. Although the chemical aspect is receiving increasing attention in recent studies, numerous processes are still the subjects of ongoing debate. A prominent example is the change of the contact angle of metal surfaces over time, the so-called 'aging effect' [38, 42]. Regarding the properties of LIPSS, particularly their orientation, Florian et al. recently demonstrated that the oxidation of the material surface plays an important role already during the formation process [43]. The laser-induced chemical modification of the material surface will be addressed in the further course of the present work for the different types of material and discussed in the context of the functional surface properties.

2.1 Formation of LIPSS on metals

The formation of LIPSS on metals was investigated for a wide range of different types [5]. In addition to titanium, molybdenum and aluminium, the reproducible fabrication of highly regular LIPSS was demonstrated, particularly on stainless steel, which is widely used in various medical applications and as implant materials, amongst others [44].

2.1.1 Influence of laser beam polarisation

Stainless steel (AISI 304; 1.4301; X5CrNi18-10) was the subject of investigations using different polarisation states of the fs-laser radiation [45]. The studies demonstrated highly regular grating structures fabricated by means of linear polarisation. Furthermore, circularly polarised radiation resulted in the formation of random structures consisting of nanodots and ripples with many intersections and bifurcations [45]. The alignment of the structures according to the beam polarisation was also investigated by studies on different focal intensity distributions realised by refractive beam shaping [46]. In addition, cylindrical vector fs-laser beams were used to produce radial, azimuthal and spiral structures in the focal spot [47–50]. The efforts for a defined control of the alignment of the structures were reinforced by various studies on stainless steel, amongst others, on structural colours [51], wettability [52] and the control of cell adhesion and migration [53], in which the strong anisotropy of LIPSS was demonstrated to be a key aspect.

Despite the promising results presented, only a few studies considered transient polarisation states during LIPSS-based surface structuring. The possibility of influencing LIPSS formation *in situ* during laser processing was demonstrated by a well-defined control of the direction of the *E*-field vector [45]. Using a polariser mounted to a motor-driven rotation device (Figure 2A), this novel flexible method allows for transferring the originally well-ordered periodic ripple pattern into structures with tailored and location-dependent orientation, thus

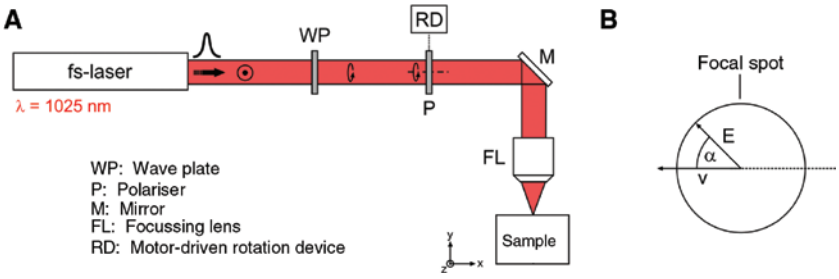

Figure 2: The (A) experimental setup and (B) definition of the angle α between the direction of the linear laser beam polarisation (*E*-field vector) and the scanning velocity *v*. Reprinted from [45], with permission from Elsevier.

facilitating the modification of the functional properties of the surface.

The structures generated in this way are similar to typical results published in the literature for stainless steel with regard to their spatial period ($\Lambda = 925$ nm) and orientation ($\perp E$) [5, 44]. The key parameter of the method is given by the rotation angle $\Delta\alpha$ of the *E*-field vector between two successive laser pulses. Starting from the highly ordered structures produced with static linear polarisation, it has been shown for different $\Delta\alpha$ -values that the LIPSS orientation is able to follow simultaneously the direction of the *E*-field vector up to relatively high rotation angles (Figure 3). Due to the constant scanning velocity, the rotation period of the generated structures decreases with increasing $\Delta\alpha$. This is highlighted by the angular-dependent optical response of the structures upon the illumination under grazing incidence. The results are discussed based on the model presented schematically in Figure 3 (bottom part) for $\Delta\alpha = 15°$. This model suggests that the first of all pulses required for LIPSS formation hits an unexposed area and generates the initial LIPSS structure owing to the interference of the excited surface plasmons with the incident laser radiation [45]. The energy of the subsequent laser pulses is then transferred to the metal surface by a 'grating-assisted' coupling and generates the finale ripple pattern [54].

At very high rotation angles, the rotation of the E-field vector between two successive pulses is too large to ensure a continuous rotation of the structures. As shown in Figure 3D for $\Delta\alpha = 28°$, the morphology and the optical response of the generated LIPSS are similar to those obtained with circular polarisation wherein the rotation frequency of the *E*-field vector corresponds to the light frequency (Figure 3E). However, the main advantage of the investigated technique when compared to structuring with circularly polarised radiation is given by the fact that the degree of disorder can be adjusted by the laser and processing parameters.

Tailored disordered structures have received renewed interest for photon management in a great variety of engineering applications. Unlike perfectly periodic or totally random structures, tailored quasi-random structures can offer both broadband absorption enhancement and customisable spectral response for different photonic devices [55]. Jwad et al. recently utilised the control of the polarisation direction online during laser processing in order to produce ripple-gratings with angular periodicity for the realisation of diffraction holograms [56]. Aside from optics, a number of other potential applications can be derived, such as the generation of superhydrophobic tracks in order to direct liquid flow along pre-defined paths, aerodynamic and tribological applications, the fabrication of surfaces with antibacterial properties [57], the control of cell adhesion and proliferation on implant materials [53] and the utilisation of this method for anti-counterfeiting applications [51]. In order to transform these approaches into an industrial solution, the change of the polarisation direction must be fully automated. A corresponding approach in connection with LIPSS formation was recently presented by Hermens et al. using a liquid crystal polariser [58].

2.1.2 LIPSS formation on metals with tailored focal intensity distributions

Tailored intensity distributions of the fs-laser radiation in the focal region are an active field of research with the aim of achieving a user-defined interaction with the material. In the context of LIPSS, beam shaping is used, amongst other things, for the homogenous large-area structuring of surfaces [59], for upscaling approaches to reduce processing time [60] and for the creation of novel biomimetic structures [47–49]. The formation of LSFL on stainless steel (AISI 316L, 1.4404, X2CrNiMo17-12-2) was investigated as a function of different focal intensity distributions using a refractive beam shaping element [46]. In combination with

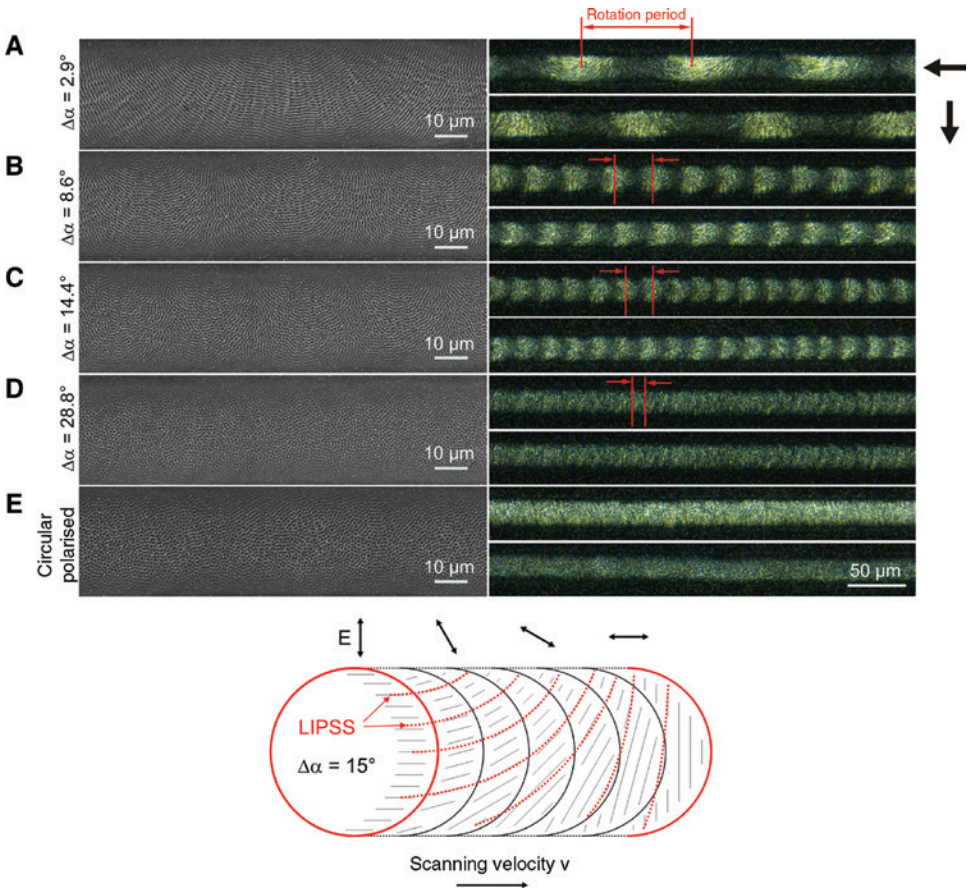

Figure 3: The surface of polished stainless steel upon the irradiation with fs-laser pulses ($F = 1$ J/cm²) utilising an *E*-field vector rotating between two successive laser pulses by an angle $\Delta\alpha$ of (A) 2.9°, (B) 8.6°, (C) 14.4° and (D) 28.8° in comparison to the utilisation of (E) circular polarisation; left: SEM micrographs and right: Optical micrographs imaged with side-illumination at grazing incidence (arrows indicate the direction of illumination); bottom: Proposed model of LIPSS formation with rotating *E*-field vector ($\Delta\alpha = 15°$). Reprinted from [45], with permission from Elsevier.

the F-Theta lens of the laser scanner, this optical element offers the possibility to convert the Gaussian intensity distribution of the output beam into tailored focal intensity distributions as illustrated in Figure 4.

Depending on the position relative to the Gaussian beam waist (z-direction), donut- and top-hat-shaped intensity profiles are provided that allow to influence the surface topography and the spatial distribution of the LIPSS within the focal spot (Figure 5). Remarkable differences are observed concerning the homogeneity of the fabricated LIPSS. Whilst the high intensive centre typical for Gaussian profiles results in extensive melt formation (Figure 5C), the top-hat profile (Figure 5D) enables the fabrication of very homogeneous LIPSS without melt formation due to the uniform intensity distribution in the beam cross-section. Moreover, the homogeneous energy deposition on the material surface by means of top-hat profiles allows for the increase in the quality and speed of the LIPSS formation process, which is realised by scanning the focused fs-laser beam over large surface areas [46, 59]. In particular, this concerns the homogeneity of the structures concerning their spatial period and alignment which, in turn, determines the resulting functional properties, such as structural colours [46].

2.2 Formation of LIPSS on graphite

The LIPSS formation on graphite was investigated in detail on bulk materials based on the polarisation state and other influencing parameters [34, 61–64]. Beyond the state of the art, the formation process was also studied on carbon fibres prepared from polyacrylonitrile (PAN) and pitch precursors [41, 65]. They provide substrates with a strongly curved surface due to the fibre diameter of about 10 µm. This is an interesting aspect as the radius of curvature is not much larger than the LIPSS spatial periods resulting from the utilised laser wavelength $\lambda = 1025$ nm.

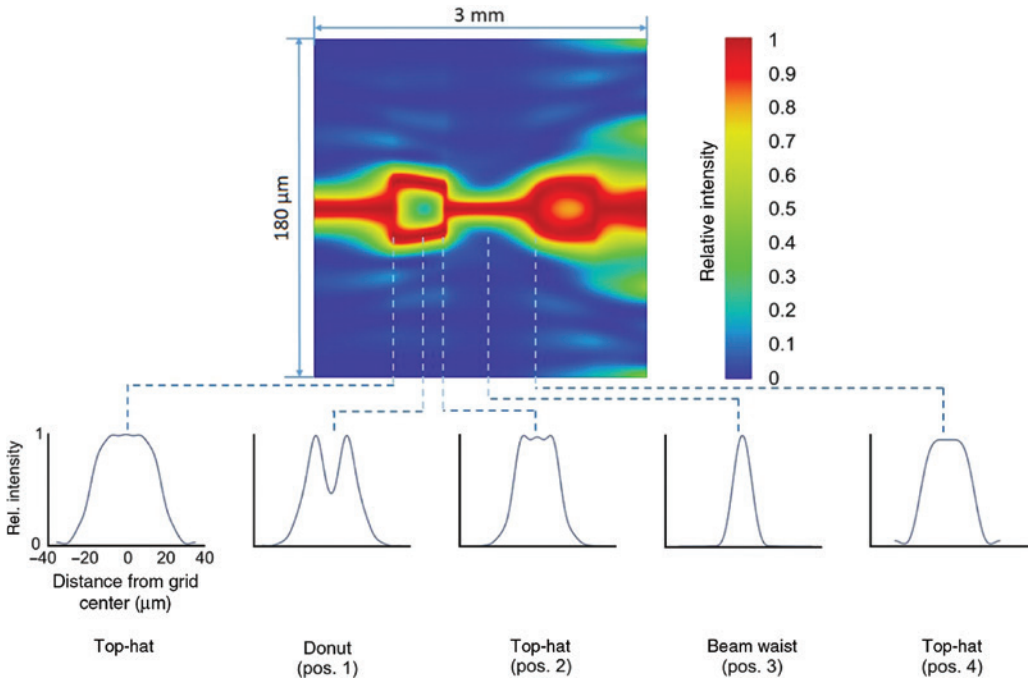

Figure 4: The visualisation of the normalised beam profiles along the *z*-direction in a range of ±1.5 mm around the focal plane and corresponding beam profiles for the different planes. The focusing lens is characterised by a focal length $f_L = 100$ mm and a numerical aperture $NA = 0.05$ at 780 nm [46].

Moreover, from the practical point of view, the interface between the fibres and the surrounding matrix determines the properties of the fibre-reinforced polymers (CFRP) and concretes (ECC). Compared to conventional, mostly chemical methods, the great advantage of laser-based structuring is provided by the precise adaptability of the LIPSS properties, particularly the spatial period and orientation of the structures relative to the fibre axis [41, 65]. This aspect, in combination with the unaffected mechanical properties, enables a systematic investigation of the properties of the fibre-matrix interface and their impact on the performance of fibre-reinforced composites.

In addition, it is conceivable to transfer the knowledge gained for the processing of strongly curved surfaces to polymer- or glass-based optical fibres. Potential applications are then given in the defined coupling and extraction of light into/from the optical fibres (light management), whereby a major advantage over conventional methods lies in the selectivity of the structuring method. In addition, the structured fibres have great potenial for application in the production of fibre-based sensors.

2.2.1 Laser-mater interaction at strongly curved surfaces

The fundamental processes of LIPSS formation on carbon fibres were studied by means of single-spot experiments with linearly polarised radiation and Gaussian focal intensity distribution (Figure 6) [65]. Depending on the exact position in the intensity profile, both HSFL and LSFL are observed on the fibre surface (Figure 6A) and both are characterised by an orientation perpendicular to the linear beam polarisation, corresponding to the results received on bulk graphite materials [63]. Whilst the LSFL exhibit spatial periods close to the incident laser wavelength ($\Lambda_{LSFL} \sim 860$ nm), the HSFL are characterised by much smaller periods ranging from 130 nm–240 nm. The ability to generate LSFL parallel and perpendicular to the fibre axis *A* with almost identical Λ_{LSFL} is demonstrated by rotating the linear polarisation by 90° relative to *A* (Figure 6B, C). Following Sipe theory [14] (see Ch. 2), a study reported that the spatial periods and the orientation of the LSFL can be predicted very well by taking into account the transient excitation of the material via the Drude approach [41]. However, in accordance with the literature, this model is not suitable for describing the HSFL properly. In contrast to the formation of random structures reported by Huang et al. for graphite bulk materials at normal incidence [66], the illumination of the carbon fibres with circularly polarised radiation leads to the simultaneous appearance of both LSFL directions (Figure 7A). The dominating direction depends on the specific position at the fibre surface. These findings are a result of the geometrical anisotropy of the fibres and

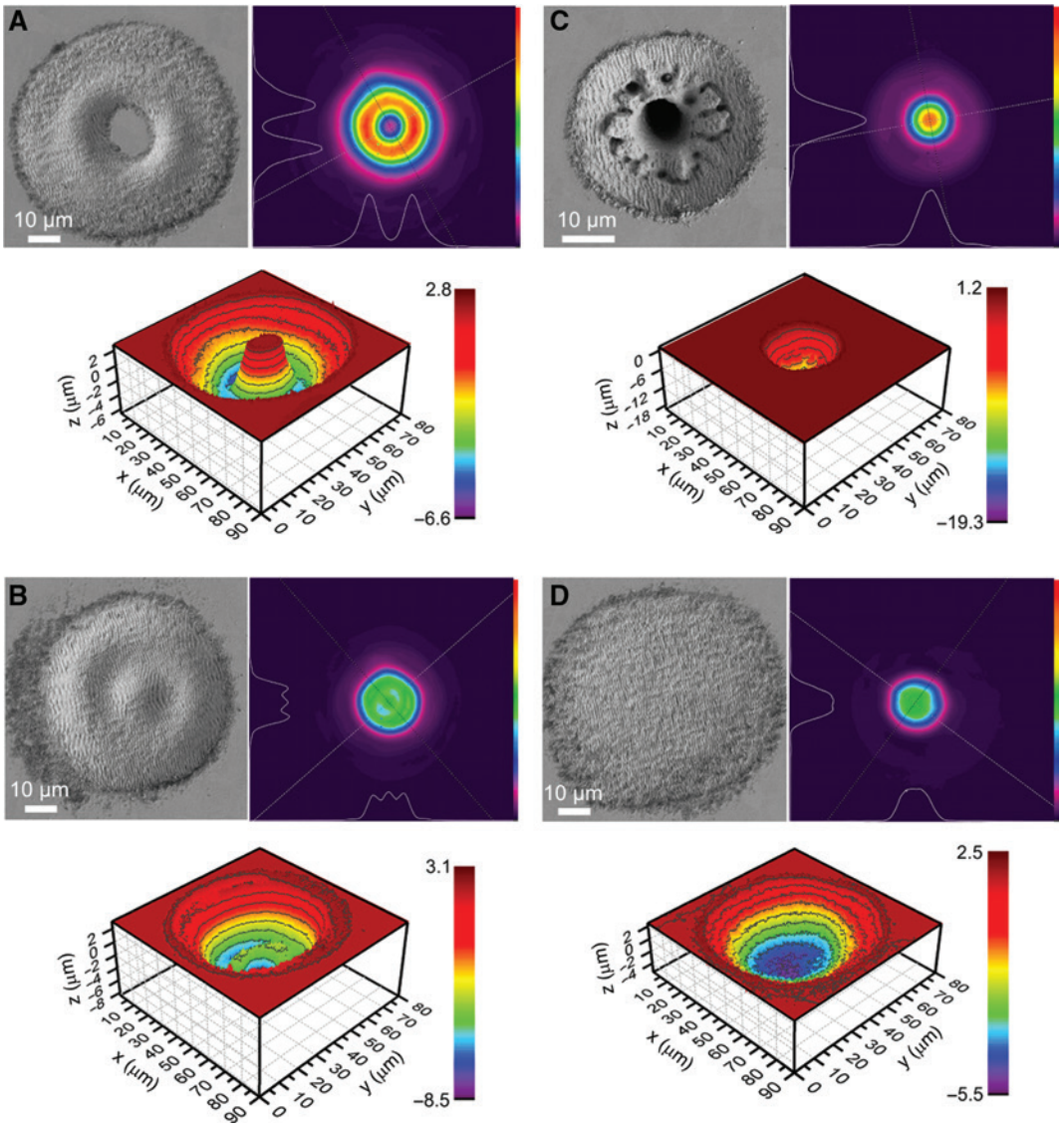

Figure 5: The comparison of calculated focal intensity distributions with SEM micrographs and WLIM micrographs of the ablation spots fabricated with $N = 200$, $E_{imp} = 13$ µJ and the corresponding intensity profiles: (A) donut (pos. 1), (B) top-hat (pos. 2), (C) Gaussian beam waist (pos. 3) and (D) top-hat (pos. 4). Note the different scaling of the colour bars in the WLIM micrographs, which indicate the determined ablation depth in µm [46].

are explained by the polarisation-dependent absorption (Figure 7B) [67].

2.2.2 Large-area fabrication of LIPSS on carbon fibres

The implementation of specific applications of the structured carbon fibres requires the production of large areas with homogeneously distributed LIPSS without a negative impact of the intensive fs-laser irradiation on the fibre properties. This concerns, in particular, the reduction of the fibre diameter due to excessive ablation and the laser-induced modification of the chemical composition on the fibre surface [68, 69]. Considering these aspects, the large-area nanostructuring of the fibres with HSFL and LSFL, respectively, was investigated based on the exact adjustment of the relevant parameters evaluated from optimisation experiments (Figure 8) [41].

The surface height profiles of both LIPSS types exhibit modulation depths of about 150 nm, corresponding in the valleys of the LIPSS pattern to a reduction of the fibre diameter of ~3% and of the effective cross-sectional area of ~6%. The uniformity of both LIPSS types on an area of about (5×1) cm^2 is underlined by the optical response of the fibre arrangement (Figure 8C, F). The exact response depends on the respective spatial periods. For HSFL, the

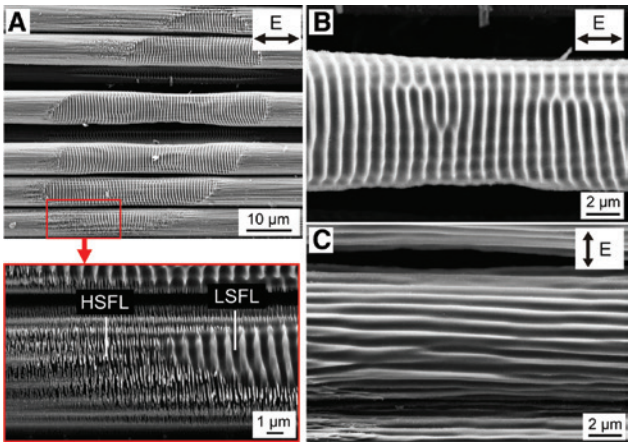

Figure 6: The SEM micrographs of LIPSS at the surface of carbon fibres: (A) HSFL and LSFL fabricated within the focal spot using linear polarisation parallel to the fibre axis; (B, C) LSFL fabricated with linear polarisation parallel and perpendicular to the fibre axis, respectively. Adapted with permission from [65] © The Optical Society.

scattering effects result in a reduced reflectance of the material surface [70] and LSFL lead to the appearance of the typical structural colours (see Ch. 3.1). At low fluences required for the HSFL formation, a selective onset of the LIPSS formation is demonstrated in the grooves of the production-related morphology of the initial fibre surface. Whilst the increase in F leads to a remarkable increase in Λ_{HSFL}, the spatial period is almost independent of F in the case of the LSFL. This behaviour was already observed in the single-spot experiments with Gaussian intensity distribution [65] and was also reported for other materials [71].

The material structure and surface chemistry of the carbon fibres before and after fs-laser irradiation were studied by micro Raman spectroscopy and XPS [41]. Despite the higher fluence required for LSFL formation, the utilised methods reveal almost similar properties of the fibres structured with HSFL and LSFL, which can be attributed to the much lower number of laser pulses in the case of LSFL. An increased structural disorder in the graphite crystalline structure was measured as a result of the fs-laser irradiation (Figure 9A). This is indicated by an increase of the ratio I_D/I_G of the D (1355 cm^{-1}) and G (1585 cm^{-1}) peak intensities and the respective peak widths caused by LIPSS formation [68, 69]. XPS analysis also reveals a reduction of the amount of sp^3 type of carbon (C-C sp^3 at 285.0 eV) evaluated at the fibre surface after fs-laser irradiation (Figure 9B). This agrees well with the introduced disorder in the sample found by the rise of the D peak in the Raman spectra. Moreover, the creation of additional C=O bonds is indicated by an increasing signal at a binding energy of about 288 eV, which is supported by the broadening of the O1s peak in Figure 9C.

2.3 Formation of LIPSS on silicate glasses

The formation of LIPSS on glasses was mainly investigated for fused silica considering a large variety of influencing parameters including laser wavelength λ, laser peak fluence F, pulse number N and beam polarisation [71]. These studies were extended by systematic analyses of the formation process on commercially available samples of different silicate glasses (fused silica, borosilicate glass and soda-lime-silicate glass) as a function of the material properties (e.g. chemical composition) at normal incidence and in air atmosphere [9, 10].

2.3.1 Influence of chemical composition

Single-spot experiments demonstrate that, generally, both types of LIPSS (HSFL and LSFL) can be generated on all

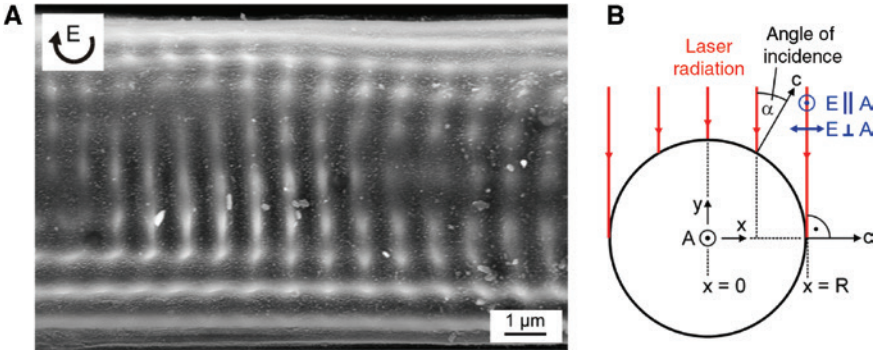

Figure 7: (A) SEM micrograph of LSFL fabricated on a carbon fibre with circular polarisation and (B) irradiation geometry due to the strongly-curved fibre surface; *A*: fibre axis, *R*: fibre radius. Adapted with permission from [65] © The Optical Society.

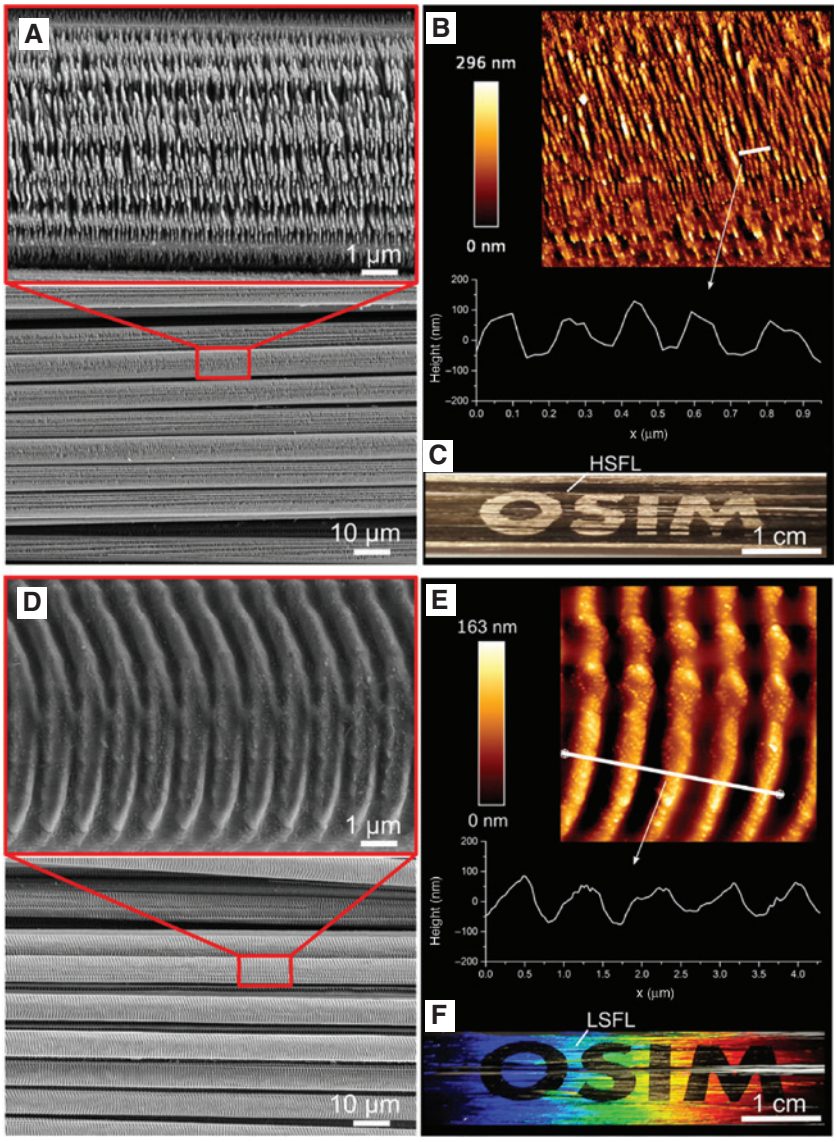

Figure 8: Large-area fabrication of (A–C) HSFL ($F = 0.7$ J/cm², $v = 0.23$ m/s, $\Delta x = 2$ µm, $N = 89$) and (D–F) LSFL ($F = 4.8$ J/cm², $v = 0.63$ m/s, $\Delta x = 6$ µm, $N = 12$) on carbon fibres. SEM micrographs reveal the morphology of the fibre surface (A, D), AFM micrographs and height profiles illustrate the surface topography (B, E) and photographs demonstrate the homogeneity of the grating structures on large areas in the cm² range (C, F). Reprinted from [41], with permission from Elsevier.

of the investigated silicate glasses by the selective ablation of the substrate surface (Figure 10A–I) [10]. However, the threshold fluence for the formation of LSFL ($N = 5$, $f_{rep} = 1$ kHz) differs from 3.4 J/cm² for soda-lime-silicate glass over 4.1 J/cm² for borosilicate glass to 5.1 J/cm² for fused silica.

This difference in behaviours was discussed based on the band gap energies experimentally determined by transmission spectroscopy and the energy density required to dissociate the oxidic composition of the glasses into their atomic components [72–74]. In the case of fused silica as the well-studied reference system (Figure 10A–C), the generated structures are in line with literature in terms of their type, spatial period and orientation, whereby a direct comparison to other works is complicated by deviating wavelengths, pulse numbers and pulse durations [71].

The lowest fluence $F = 5$ J/cm² leads to the formation of HSFL, which are characterised by spatial periods Λ_{HSFL} ranging from 200 nm–400 nm ($0.19 \cdot \lambda$–$0.39 \cdot \lambda$). In this case, the specific value of Λ_{HSFL} depends on the local fluence correlated to the Gaussian intensity distribution of the fs-laser beam. The increase in F results in the formation of LSFL in the centre of the Gaussian beam profile

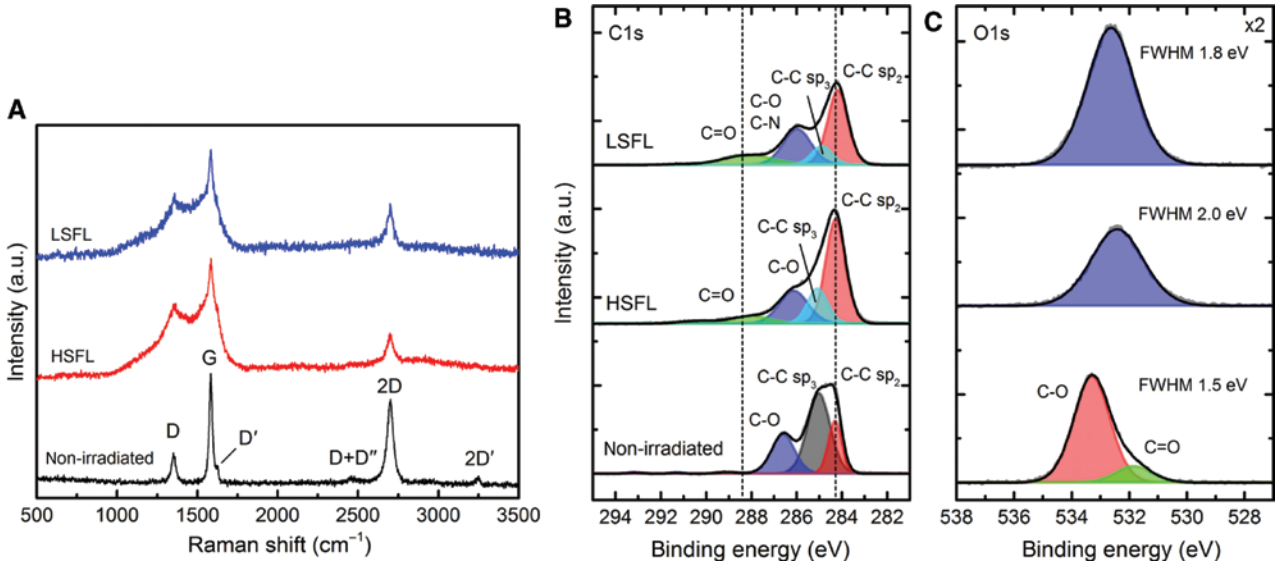

Figure 9: (A) Raman spectra and (B, C) XPS spectra of non-irradiated fibres compared to fibres covered with HSFL ($F = 0.7$ J/cm², $N = 89$) and LSFL ($F = 4.8$ J/cm², $N = 12$), respectively. Reprinted from [41], with permission from Elsevier.

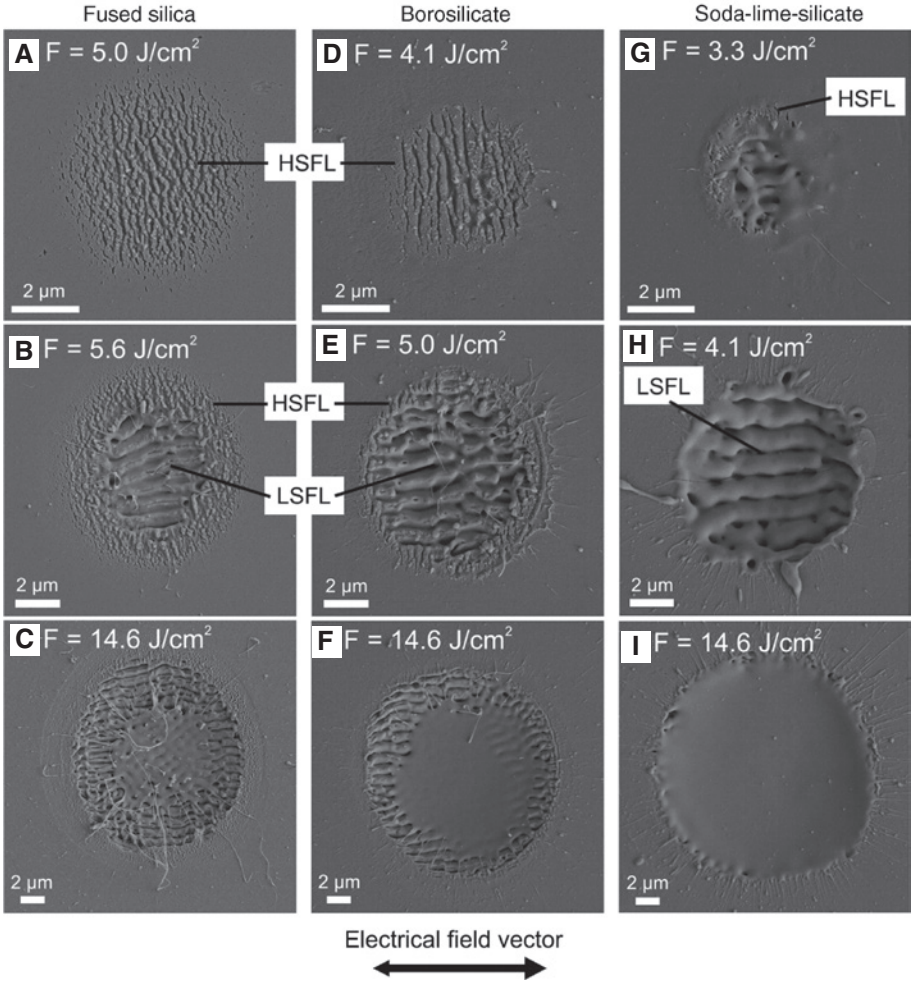

Figure 10: The SEM micrographs of the surface of (A–C) fused silica, (D–F) borosilicate glass and (G–I) soda-lime-silicate glass upon irradiation with $N = 5$ linearly polarised laser pulses of different peak fluence F at a repetition frequency $f_{rep} = 1$ kHz. Note the direction of the E-field vector and the different scaling of the micrographs, which was chosen in order to display the entire ablation spot [10].

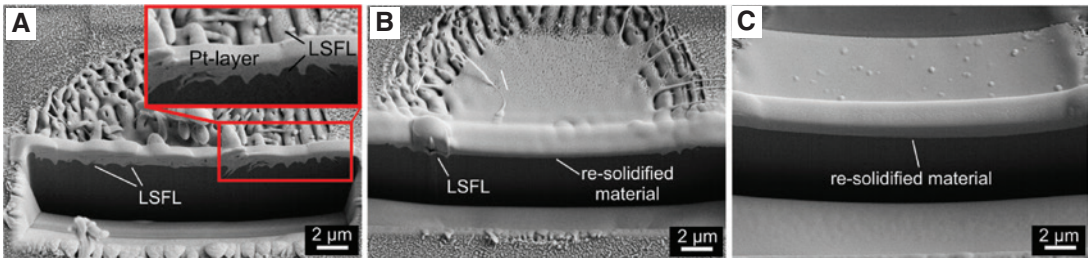

Figure 11: The FIB cross-sections prepared from the ablation spots containing LSFL fabricated with $F = 14.6$ J/cm² on (A) fused silica, (B) borosilicate glass and (C) soda-lime-silicate glass [10].

with Λ_{LSFL} increasing from 735 nm to 890 nm (Figure 12), which are surrounded by a ring-shaped area containing HSFL. The HSFL are aligned perpendicular and the LSFL are parallel to the direction of the *E*-field vector of the linearly polarised fs-laser radiation.

This configuration can be explained by the model calculations of Rudenko et al. [37] (see Ch. 2) who demonstrated that the LIPSS types are created by interference effects in different material depths. Consequently, the LSFL, which are situated deeper in the bulk, are exposed in the intensive centre of the Gaussian beam due to a stronger ablation. Considering the deviating fluence ranges, results show that the LIPSS formation on borosilicate glass (Figure 10D–F) and soda-lime silicate (Figure 10G–I) occurs principally in a way that is equal to fused silica. Significant differences, however, are observed in the amount of melt formation, which is the strongest for soda-lime-silicate glass. For this glass, the following significant effects can be observed:

1. Even at the lowest fluence value of $F = 3.3$ J/cm², HSFL are only barely visible due to the molten and re-solidified surfaces.
2. The morphology of LSFL fabricated with $F = 4.1$ J/cm² differs remarkably from that of LSFL on borosilicate glass and fused silica, generated with the corresponding fluences required for LSFL formation ($F > F_{th}$).
3. At the maximum fluence provided by the fs-laser system ($F = 14.6$ J/cm²), LSFL can no longer be observed because the molten material covers the total ablation spot.

The comparison of the glasses at $F = 14.6$ J/cm² (maximum fluence of the fs-laser system) revealed that LSFL are visible on fused silica almost in the entire ablation spot due to the weak melt formation, whereas LSFL on borosilicate glass are limited to the less intensive area of the ablation spot. In this context, the prepared focused ion beam (FIB) cross sections in Figure 11 exclude the possible sub-surface LIPSS that might be covered with a thin melt layer. Instead, the results revealed a very flat surface without any LIPSS-like modulations in this centred area. These results suggest an intense heating in the centre of the ablation spot leading to melt formation and a reduction of the temperature-dependent viscosity [10].

A detailed evaluation of the ablation spots as a function of *N* indicates that the melt formation is a single-pulse effect. The contribution of inter-pulse effects to the melt formation, such as heat accumulation resulting from the sequential impact of several laser pulses, was excluded by experiments with different values of f_{rep} ranging from 1 Hz–100 kHz (i.e. the temporal pulse separation varied between 10 µs and 1 s) [10].

The spatial periods Λ_{LSFL} measured on fused silica and borosilicate glass by two-dimensional-Fourier transformation (2D-FT) are smaller than the laser wavelength λ, whilst soda-lime-silicate glass exhibits periods exceeding λ (Figure 12) [10]. The formation of LIPSS on different glasses was theoretically calculated using Sipe theory [10, 14]. For fused silica, a Drude damping time of $\tau_D = 0.4$ fs and an optical effective mass of $m_{opt} = 0.49$ have been demonstrated to be suitable parameters [75].

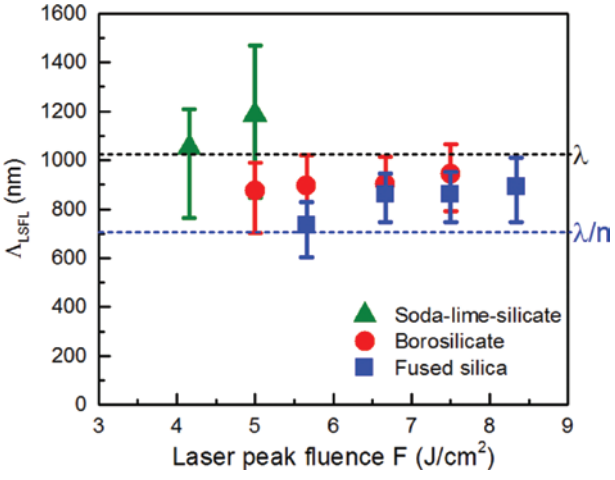

Figure 12: The spatial periods of LSFL on various glasses determined from the SEM micrographs by 2D-FT in dependence of *F* [10].

The efficacy factor maps (η-maps) calculated for fused silica as a function of N_e confirm the suitability of the electromagnetic approach in explaining the sub-wavelength characteristics of the spatial periods and the orientation of LSFL (Figure 13). Considering the smaller band gap and thus a stronger excitation of the material, it has been shown that the calculations can also be used to explain the LIPSS properties on borosilicate glass, although the optical input parameters (i.e. the refractive indices) are almost identical. However, Sipe theory fails to predict the supra-wavelength LIPSS observed on soda-lime-silicate glass. According to Sipe theory, LSFL with spatial periods almost as large as the laser wavelength would require a very strong excitation of the glass that corresponds to a metallic-like state of the material, which results in an alignment of the LSFL perpendicular to the beam polarisation [71]. As the main difference in LIPSS formation on the different glasses lies in the strong melt formation on soda-lime-silicate glass, this indicates that hydrodynamic processes are involved in LIPSS formation as suggested by some authors [24–26]. In this context, the following aspects may have to be considered:

1. The hydrodynamic processes (e.g. Marangoni convection) require melt formation, which is successfully demonstrated in the present work for soda-lime-silicate glass (Figure 10G–I).
2. The contribution of hydrodynamic processes requires a sufficient lifetime of the material in its molten state. Corresponding investigations were conducted by Ben-Yakar et al. for borosilicate glass during fs-laser irradiation [76].
3. The viscosity of the liquid strongly influences the fluidity and laser-induced displacement of the molten material. Moreover, the viscosity of the investigated glasses varies strongly due to their different chemical composition [77].

Concerning the first point stated above, a transiently softened state is also achieved with fused silica due to the specific glass transition from the solid to the vapour state. The corresponding viscosity, however, is several orders of magnitude larger than that of the other glasses. Hence, melt formation in the form of, e.g. a visible deformation of the substrate surface is not observed. Consequently, the contribution of hydrodynamic processes is assumed to play a minor role for fused silica and to be less pronounced for borosilicate glass when compared to the soda-lime-silicate glass [10]. Thus, the findings obtained for the different glasses extend the understanding of LIPSS formation and provide an essential basis for the large-area structuring of transparent materials with LIPSS. This particularly applies to soda-lime-silicate and borosilicate glasses, which are used in numerous technical applications due to their lower price and better manufacturability.

2.3.2 Influence of initial substrate temperature

The results obtained on different silicate glasses particularly reveal that LIPSS formation is most strongly influenced by melt formation and possible hydrodynamic processes on glasses with low viscosity. Therefore, the

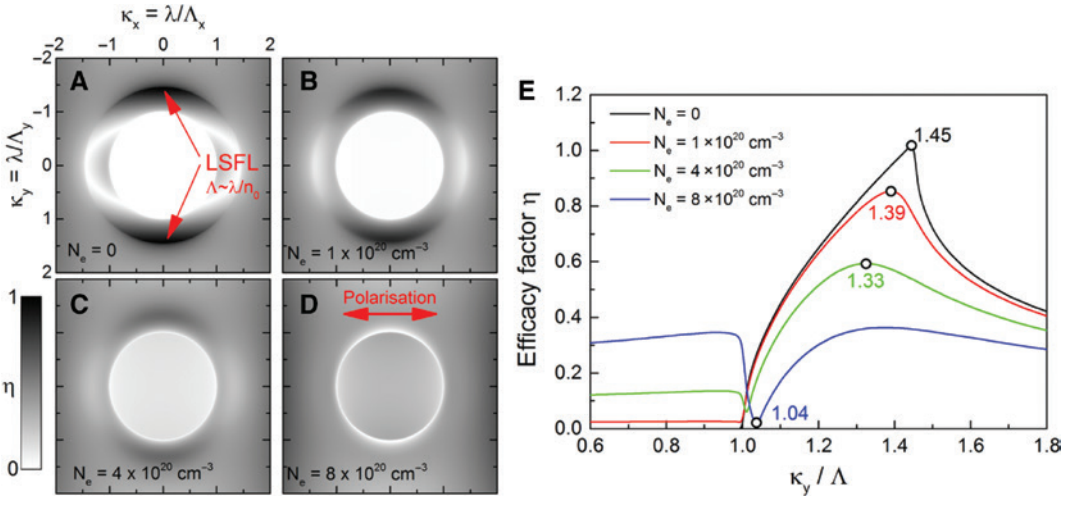

Figure 13: The theoretical analysis of LIPSS formation on fused silica: (A–D) Two-dimensional grey-scale images of η and (E) cross-sections of the η-maps along the positive κ_y-direction at $\kappa_x = 0$ as a function of the quasi-free electron density N_e [10].

influence of viscosity was evaluated on fused silica as substrate material superimposing a continuous wave (cw) CO_2 laser beam as a heating source for the fs-laser radiation (Figure 14A) [9]. Using this novel approach, single spots with LIPSS were fabricated at different, well-defined substrate temperatures T_S (Figure 14B), which enabled the systematic investigation of their evolution as a function of the temperature-dependent material parameters relevant for the interaction process (e.g. refractive index, viscosity, band gap). The studies include a detailed analysis of the optical properties of fused silica at the wavelength $\lambda = 10.6$ µm of the heating CO_2 laser radiation [78].

The corresponding LIPSS patterns obtained from the irradiation of the fused silica surface with different values of F as a function of T_S were compared to the results at room temperature T_{RT} as reference (Figure 15). At the investigated fluences, a remarkable increase of Λ_{LSFL} with increasing T_S is determined by 2D-FT (Figure 16). At the maximum investigated temperature $T_S = 1200$°C, Λ_{LSFL} reaches a value of (1170 ± 90) nm for $F = 9.28$ J/cm². At $T_S \approx 800$°C, Λ_{LSFL} is equal to the wavelength $\lambda = 1025$ nm of the fs-laser beam. For $T_S > 800$°C, the observed laser-induced structures correspond to supra-wavelength LIPSS again. Here, the spatial period exceeds λ at maximum by a factor of about 1.14 at $T_S = 1200$°C. This means that Λ_{LSFL} increased by about 36% when compared to T_{RT}. For the processing conditions, the slope $d\Lambda/dT$ is found to be $0.24\ nm \cdot K^{-1}$.

2.3.3 Hydrodynamic aspects of LIPSS formation on glasses

In order to theoretically explain the obtained results, especially with regard to the observed supra-wavelength LIPSS, the established Sipe theory procedure (see Ch. 2) was modified to identify effective dielectric permittivities ε^* at which the sub- and supra-wavelength periodic energy deposition could be obtained [9]. Consequently, η-maps were calculated for given structural sizes in the space of complex dielectric permittivities [Re(ε), Im(ε)]. On the one hand, the respective calculations demonstrate the suitability of Sipe theory in describing the sub-wavelength (LSFL) structures generated at T_{RT}, whilst considering the Drude approach, which is in line with previous model calculations [10, 22]. On the other hand, the excitation of supra-wavelength LIPSS is possible, in principle, on fused silica, but only under conditions that cannot be achieved either by transient excitation of the material in the sense of the Drude model or by a change in the optical constants (i.e. refractive index n and extinction coefficient k) caused by a temperature increase of the substrate. The latter is mainly due to the small change of the refractive index of fused silica with temperature ($dn/dT = 1.15 \cdot 10^{-5}\ K^{-1}$) [79]. Thus, the obtained experimental results, particularly the supra-wavelength LIPSS and the increase of Λ_{LSFL} with T_S, are not adequately described by Sipe theory.

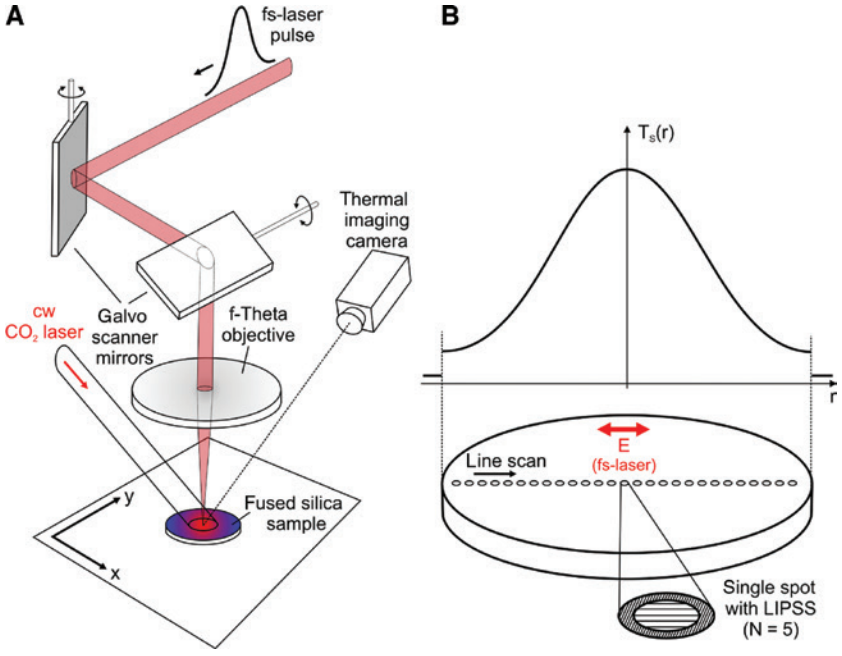

Figure 14: The (A) experimental setup and (B) generation of LIPSS as a function of the substrate temperature T_S that depends on the radial position on the sample surface [9].

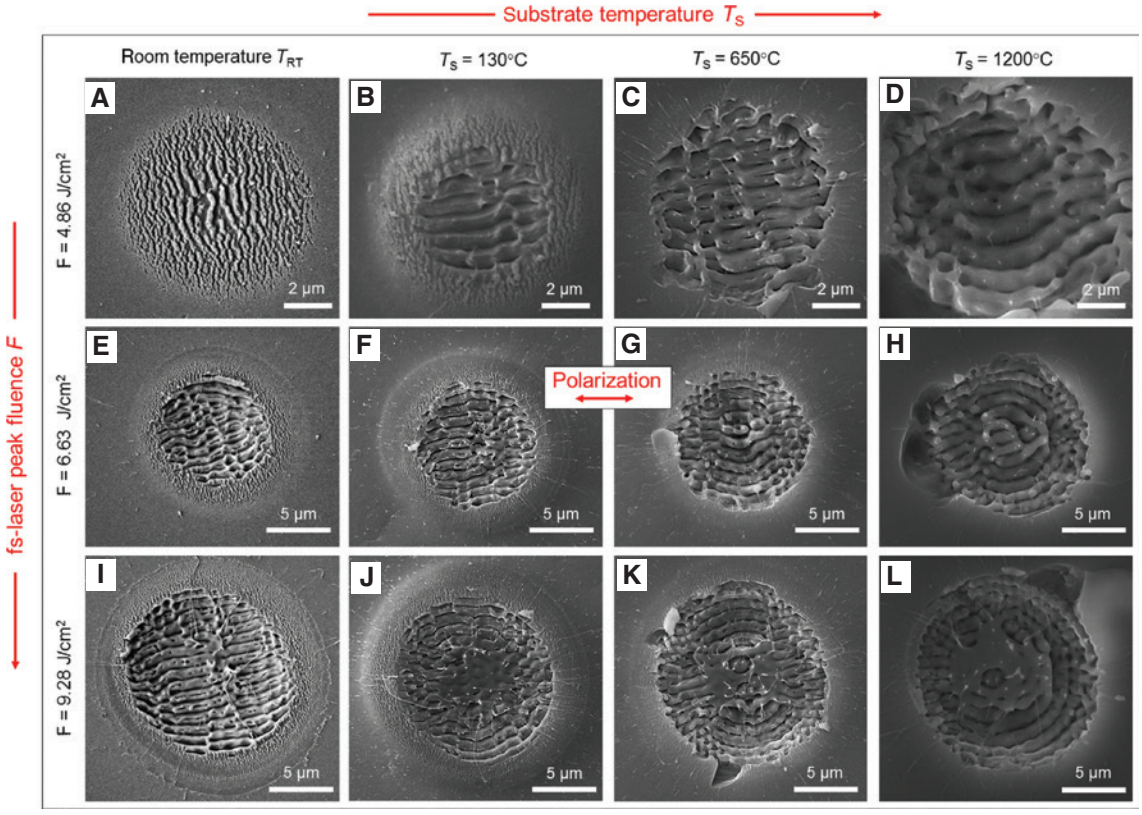

Figure 15: SEM micrographs of the fused silica surface upon irradiation with linearly polarised fs-laser pulses ($N=5$) at T_{RT}, $T_S=130$°C, 650°C and 1200°C using (A–D) $F=4.86$ J/cm², (E–H) $F=6.63$ J/cm² and (I–L) $F=9.28$ J/cm². Note the direction of the beam polarisation (red arrow) and the different scaling of the SEM micrographs [9].

As the experimental results indicate that the effect of melt formation and viscosity is more relevant than the transient change of the optical properties, hydrodynamic studies are performed using non-dimensional numbers analysis [27] in order to predict hydrodynamic instabilities that may occur in the laser-induced molten fused silica layer after irradiation. The corresponding results suggest that convective transport dominates the diffusive transport of the liquid and that the free surface of the hot liquid can be rapidly deformed by temperature-dependent surface tension gradients [9].

The results also suggest that a thermo-convective instability, driven by the surface tension modification, may be acting in the molten layer after undergoing laser irradiation [9]. This effect was quantified by applying a model of thermo-convective transport in order to calculate possible periodicities that can emerge by the development of thermo-capillary instabilities in the hot molten fused silica layer with a free surface [28]. Using this model, a growth rate γ of this thermo-capillary instability was calculated that depends on the liquid molten layer thickness h, the material temperature T, the temperature-dependent surface tension $\sigma(T)$ and the temperature-dependent viscosity $\eta(T)$. Figure 17 shows the growth rate γ of the thermo-convective instability as a function of the mode periodicity Λ calculated for $T=2000$ K. Evidently, the period of the fastest developing mode increases with increasing h and the period of the most unstable mode is the supra-wavelength when the molten layer thickness exceeds 150 nm [9]. Above this layer thickness, Figure 17 reveals values of γ in the order of 10^{10}–10^{12} s^{-1}. They correspond to time durations γ^{-1} ranging from 10^{-12} to 10^{-10} s (i.e. 1–100 ps), which are smaller compared to melt lifetimes in the order of µs calculated for the fs-laser ablation of glasses [76, 80]. Thus, a fluid flow would have enough time to move the molten material. In this context, the following impacts of the CO_2 laser substrate heating seems plausible:

1. The heating causes a modification of the temperature gradients on the substrate surface, which leads to smaller cooling rates and an increased melt lifetime.
2. The thickness of the molten fused silica layer increases with increasing initial substrate temperature T_S, which, according to Figure 17, correlates with the experimentally determined increase of Λ_{LSFL} with T_S.

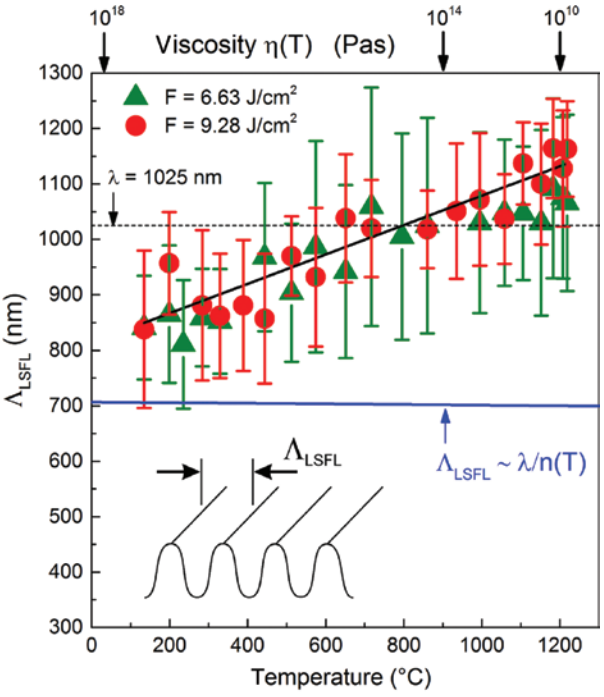

Figure 16: The spatial period Λ_{LSFL} of LSFL on fused silica ($N=5$) as a function of the initial substrate temperature T_S. The vertical bars indicate the width of distribution of the corresponding 2D-FT operation and the black solid line guides the eye. The blue line corresponds to the spatial periods Λ_{LSFL} predicted by the Sipe theory taking into account a temperature-dependent refractive index n [9].

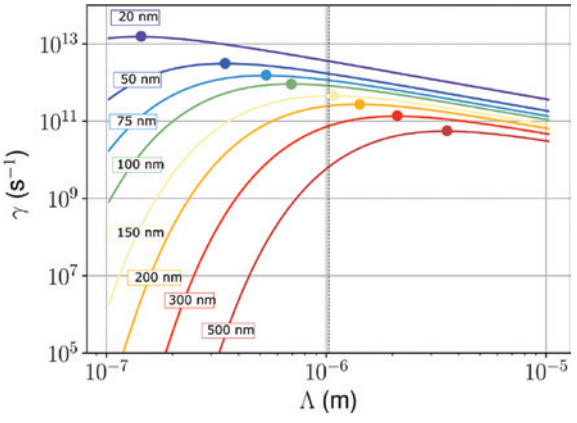

Figure 17: The growth rate γ of the thermo-convective instability as a function of the spatial period of the unstable mode calculated for thin layers of fused silica at $T=2000$ K. The dots identify the most unstable mode varying the layer thickness h from 20 to 500 nm [9].

Consequently, a hydrodynamic instability of thermo-convective nature helps explain the supra-wavelength LIPSS observed on the surface of laser-heated fused silica. However, a direct comparison of the theoretical and experimental results remains difficult due to the fact that influencing effects, such as ablation, are neglected in this study. Notably, the electrodynamic interaction of the laser radiation with the material (e.g. described by Sipe theory) may act as seed for the hydrodynamic instabilities, which can then be used to explain the orientation of the structures [24, 25].

The experimental design in combination with the specific material properties of fused silica reveals a connection between electromagnetic interaction and hydrodynamic effects, whereby LIPSS formation is increasingly dominated by hydrodynamic effects as T_S increases and viscosity decreases. This fact is supported by the transition in the alignment of the LSFL in Figure 15 starting from lower temperatures wherein they exhibit an orientation parallel to polarisation (in line with Sipe theory), to elevated temperatures (e.g. $T_S > 650$°C in Figure 15K, L), where they are characterised by a concentric alignment according to the boundary conditions given by the solid border of the ablation crater.

2.4 Formation of LIPSS on the composites

The structuring of composite surfaces with LIPSS has not been the main focus of research activities so far. However, the different absorption behaviours of the involved components and the resulting differences in the ablation thresholds offer the possibility of the selective structuring of the composite surface. The corresponding approach is based on the exact adjustment of the process and laser parameters, particularly the effective pulse number N_{eff} and the fs-laser peak fluence F, to provide a local effective laser fluence, which lies between the threshold fluences of the composite components [6–8]. By scanning the fs-laser beam with the scanning velocity v across the composite surface, LIPSS are only generated on the material areas where the respective threshold fluence is exceeded (Figure 18A). Consequently, very different, location-dependent surface properties can be generated, resulting in strongly heterogeneous surface properties concerning, e.g. wettability, optical behaviour and chemical composition.

In addition, the LIPSS-structured surface areas can be reduced to areas that are much smaller compared to the focal spot size of the processing beam. This, in turn, is equivalent to a higher resolution of the nanostructuring process. Finally, composites provide very interesting model systems to investigate the fundamentals of the LIPSS formation. This particularly concerns the formation process at the interface between the components, as materials with very different electrical and optical properties can be combined.

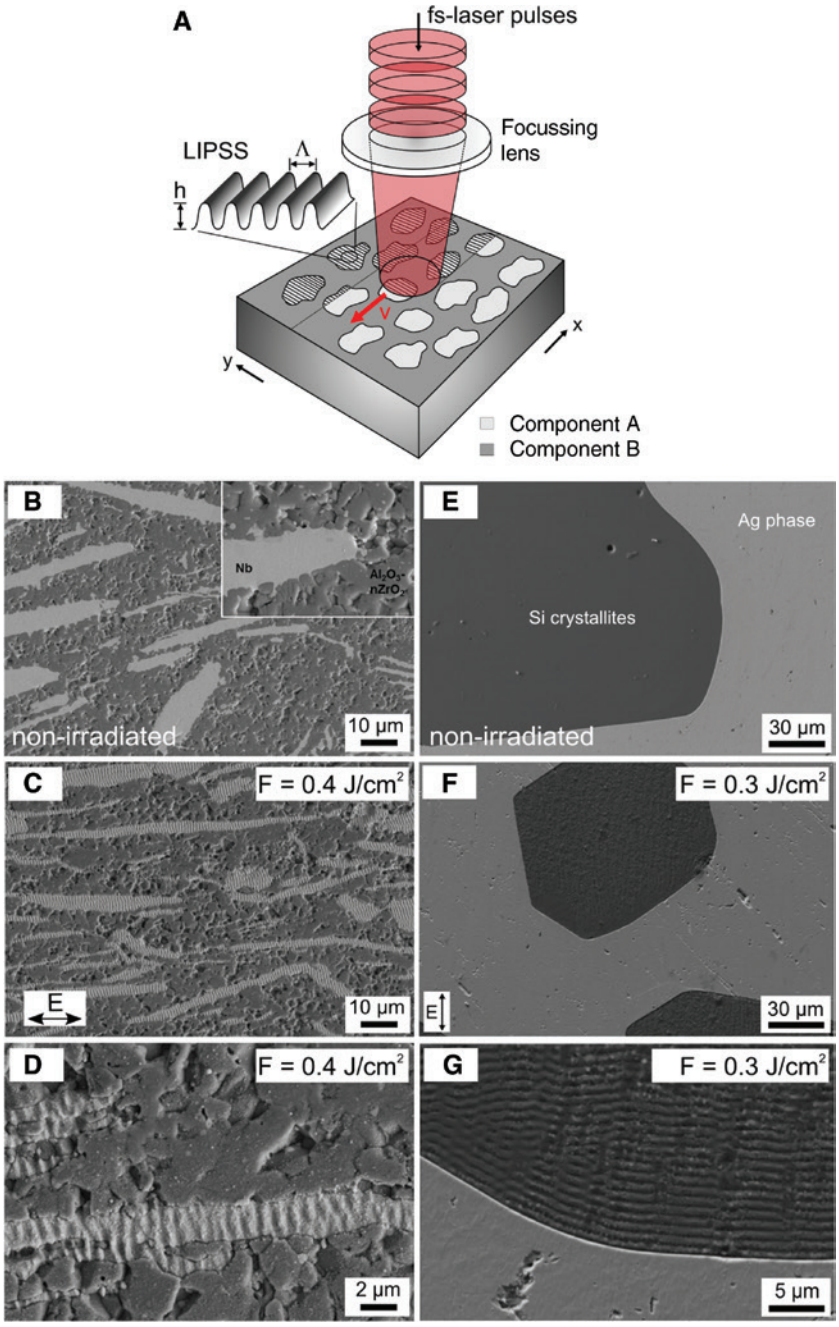

Figure 18: The selective LIPSS formation on composites by scanning a fs-laser beam with the scanning velocity *v* across the sample surface: (A) The principle of laser processing with the resulting topography that is characterised by the spatial period Λ and the modulation depth (peak-to-valley height) h. (B–G) The SEM micrographs of composite surfaces before and after fs-laser irradiation ($\lambda = 1025$ nm, $\tau_{imp} = 300$ fs) showing the selective LIPSS formation on (B–D) metal-ceramic matrix composites ($F = 0.4$ J/cm², $f_{rep} = 1$ kHz, $v = 4.4$ mm/s, $\Delta x = 4.4$ µm) and (F–G) on metal-semiconductor composites ($F = 0.3$ J/cm², $f_{rep} = 100$ kHz, $v = 0.67$ m/s, $\Delta x = 6$ µm). The polarisation direction is indicated in (C) and (F). Reprinted from [7], with permission from Elsevier and reprinted with permission from [8]. Copyright (2019) American Chemical Society.

The studies concerning the selective formation of LIPSS were performed with Al_2O_3-$nZrO_2$-Nb as representatives of the metal-ceramic-matrix composites (Figure 18B–D) [6, 7]. It consists of an alumina (Al_2O_3) matrix with an embedded metallic Nb phase in the form of µm-sized flakes with a preferred orientation resulting from the fabrication process of the material [6, 81]. The second material system is given by the Ag-Si composite, a metal-semiconductor composite consisting of silicon (Si) crystallites (average diameter of about 175 µm) surrounded

by a metallic silver (Ag) phase (Figure 18E–G) [8]. As an advantage, this material system provides the possibility of controlling the crystallite size by thermal treatment [8]. For the exact synthesis routes of both composites and the resulting properties, the reader is referred to the literature [8, 81].

Due to its specific composition, Al_2O_3-nZrO_2-Nb shows significantly better mechanical properties than pure ceramics [81–83] and can thus be used, amongst other things, as an implant material. For this composite, the selective LIPSS formation was studied in detail as a function of different laser parameters [6].

Results show that well-pronounced LIPSS selectively arise on the Nb-flakes upon fs-laser irradiation with $F = 0.4$ J/cm² (Figure 18A–C). As is typical for metals, the LIPSS are characterised by their alignment perpendicular to the linear beam polarisation (Figure 18C). The spatial period was determined by AFM and SEM to be $\Lambda \sim 750$ nm. Furthermore, the studies demonstrated an increase of the LIPSS modulation depth (peak-to-valley height) with increasing F up to a value of $h \sim 250$ nm for the LIPSS shown in Figure 18C. In this context, the increasing modulation depth is accompanied by an increase in the arithmetic mean roughness value measured on the Nb-flakes [6]. The laser-induced modifications of the ceramic matrix in terms of oxidation and phase transitions were excluded amongst others by FTIR and XPS. As a further result, the XPS analysis reveals a modification of the native oxidation layer found on the Nb-flakes before fs-laser irradiation (Figure 19) [7]. The resulting laser-induced oxidation layer is characterised by an increased thickness. Moreover, a transition from Nb_2O_5 as the most prominent oxide before fs-laser irradiation to NbO after LIPSS formation with $F = 0.4$ J/cm² is observed (Figure 19D).

The selective generation of LIPSS on the Ag-Si composite occurs similarly to the ceramic–matrix composites. The smaller threshold of Si when compared to the metallic Ag matrix leads to the selective formation of LIPSS on the semiconductor, i.e. on the Si crystallites [8]. In accordance with the literature, the alignment is typically perpendicular to the E-field vector [5]. The LIPSS are characterised by spatial periods of $\Lambda \sim 950$ nm and a modulation depth of $h \sim 220$ nm, which are comparable to values reported for bulk silicon while considering the laser parameters used. The EDX measurements of the surface revealed the laser-induced formation of silicon oxide, which can be explained by the fs-laser irradiation at normal air atmosphere [40, 84]. However, a laser-induced modification of the chemical composition of the Ag surface was not detected [8].

3 Functional surface properties based on LIPSS

LIPSS have attracted particular interest because of their great potential to create manifold functional surfaces for various technical applications [1–4]. Here, researchers are often inspired by nature, which has developed numerous outstanding skills and structures to ensure the survival of animals and plants [2, 85, 86].

3.1 Optical properties

The impact of LIPSS on the optical properties of different material surfaces was mainly investigated with regards to

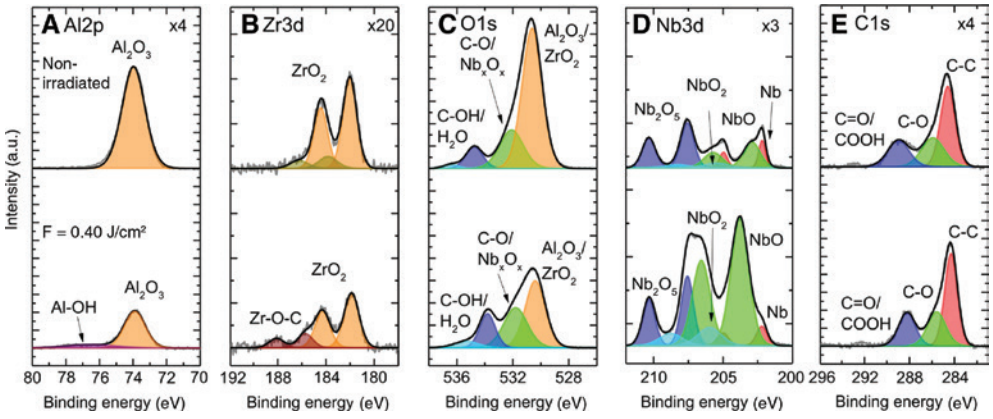

Figure 19: The high-resolution XPS spectra of the composite surface before and after fs-laser irradiation with $F = 0.40$ J/cm²: (A) Al2p peaks, (B) Zr3d peaks, (C) O1s peaks, (D) Nb3d peaks and (E) C1s peaks. Note the different multiplication factor as indicated in the spectra. Reprinted from [7], with permission from Elsevier.

the generation of structural colours [51, 87–91] along with the modification of reflection, diffraction, and absorption properties [92–96]. These studies reported that both effects are closely linked. Structural colouration is promising in providing brilliant colours, adaptive camouflage, label marking and optical data storage [3]. The structural colouration originates from the diffraction behaviours of the grating-like surface structures, which are illustrated for stainless steel in Figure 20A.

From the physical point of view, the colourising effect can be controlled by the angles of incidence θ_i and observation θ_m, the orientation φ of the ripple pattern relative to the plane of incidence (*xz*-plane in Figure 20B) and by the spatial period Λ according to $m \cdot \lambda = \Lambda(\sin \theta_i \cdot \cos \varphi + \sin \theta_m)$, with m as the diffraction order and λ as the wavelength. From the technological point of view, the versatile influencing parameters are available to modify the ripple structures and their optical response, which was demonstrated in dependence on the laser wavelength [87], the surrounding atmosphere [97] and LIPSS orientation controlled via beam polarisation [45, 51]. The optical properties of LIPSS concerning reflectivity and absorption, e.g. on metals [92, 93], fused silica [94, 98] and silicon [96], were investigated by several authors by means of integrating sphere measurements. Resulting from the anisotropic surface morphology, the reduction of light reflection is most significant for the incident polarisation parallel to the LIPSS grating vector (i.e. the *E*-field vector is perpendicular to the grooves) for both total and specular reflectance [96]. The anti-reflective effect can be further increased by the conical laser-induced surface structures ('spikes') that arise upon the irradiation with higher number of laser pulses and/or laser fluences [88, 99]. In contrast to the LIPSS, these structures are characterised by their almost broadband, omnidirectional and polarisation-independent optical response.

Beyond the state of the art, the optical response of the material surface was used as an indicator to study the behaviours of the initially well-ordered LIPSS pattern in terms of their spatial period and orientation during the plastic deformation of the substrate [100]. A central aspect in this context is the evaluation of the possibility of a subsequent well-defined manipulation of the LIPSS properties. For this purpose, stainless steel (AISI 316L, 1.4404, X2CrNiMo17-12-2) was used as substrate material and subjected to a specific thermal treatment (annealing at 1100°C for 1 h) in order to attain a uniform microstructure via recrystallisation. In the annealed state, this material is characterised by an elastic deformation limit <0.3% and a total strain ε that can significantly exceed 50%.

Based on these material properties, we expected that plastic tensile deformation of the substrate material would lead to an increase in the spatial period Λ of the LIPSS and, therefore, to a mechano-responsive change of the structural colours. In this context, a fundamental question should be clarified as to whether the plastic deformation leads to a homogenous alteration of the initially well-ordered LIPSS pattern with a linear increase of Λ or if Λ and the alignment of the LIPSS are determined by the microstructure of the material. The expected effect of increasing plastic deformation on the spatial period was confirmed by a red-shift of the structural colours that arise from white-light illumination of the structured stainless steel specimen (Figure 21). The photographical documentation reveals that this colour change is inhomogeneous, that is, it starts at specific locations that are subject to larger local strain. Figure 22 compares the corresponding surface morphology (SEM, AFM) and the microstructure of the samples (OM) as a function of the plastic deformation.

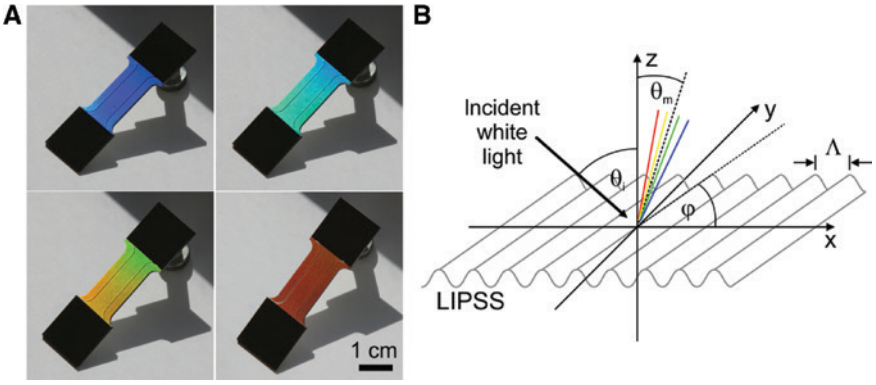

Figure 20: Structural colours on stainless steel: (A) Different colours obtained from different observation angles and (B) diffraction behaviour of the grating-like surface structures.

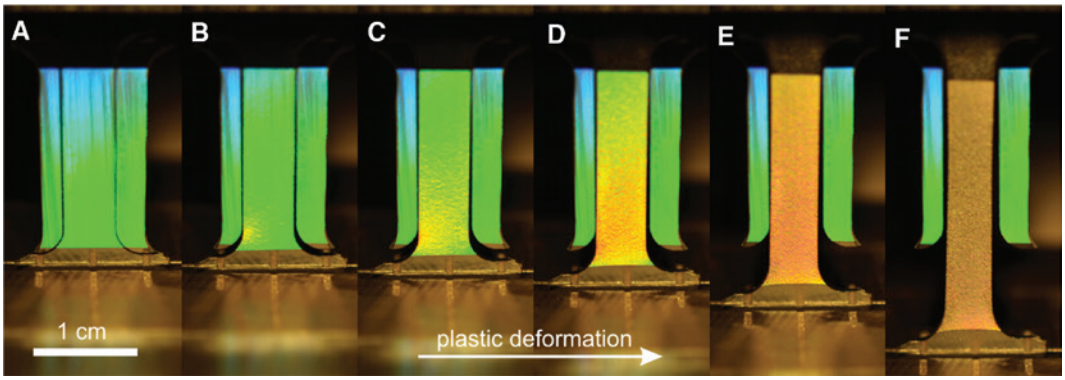

Figure 21: The structural colours resulting from LIPSS fabricated by fs-laser irradiation on the surface of stainless steel X2CrNiMo17-12-2. Plastic deformation with a total strain of (A) $\varepsilon = 0\%$, (B) $\varepsilon = 10\%$, (C) $\varepsilon = 17\%$, (D) $\varepsilon = 25\%$, (E) $\varepsilon = 39\%$ and (F) $\varepsilon = 62\%$ results in a red-shift of the structural colours. Reprinted from [100], with permission from Elsevier.

The comparison of the SEM micrographs (Figure 22A, E) reveals that the plastic deformation leads to a local reorientation of the originally well-ordered LIPSS and that the LIPSS period increased locally much stronger than estimated by assuming a simple homogenous deformation according to $\Lambda' = \Lambda \cdot (\varepsilon + 1)$. The latter results in a factor $\Lambda'/\Lambda = 1.6$ for the maximum total strain of $\varepsilon \sim 60\%$. Instead, this factor strongly depends on the location on the surface and ranges from 1 to about 2.7 (points A, B and C in Figure 22E) when compared to the initial spatial period $\Lambda = (907 \pm 26)$ nm. The broad variety of spatial periods measured within the LSFL pattern is illustrated by the broadened peak in the 2D-FT spectra (Figure 22F). Moreover, the optical micrographs confirm that the plastic deformation is distributed homogenously as a consequence of the various orientations of grains with different orientation of preferred slip systems. After plastic deformation, the LIPSS pattern exhibits a rather continuous change of orientation passing from one grain to another, resulting gradual orientation deviations of about 30°. Moreover, abrupt changes of the orientation and even discontinuities with the LIPSS pattern are observed that are likely consequences of shear bands formed locally within the grains.

Finally, the AFM analysis in Figure 22 shows a topographical modification induced by the plastic deformation. This is a consequence of the motion of dislocations during plastic deformation, which results in the formation of slip bands and a change of the orientation of individual grains [101]. From the macroscopic point of view, the modified topography leads to a reduction of the diffraction ability of the grating structures and therefore to the fading of the structural colours as observed in Figure 21F. These results clearly show that the properties of LIPSS can be modified after structuring based on a tensile straining of the substrate.

This mechano-responsive colour-change of LIPSS on metals is of particular interest for the development of novel switches, safety devices, strain gauges and the early detection of material failure. However, as the plastic deformation is irreversible, studies also focused on the ability of metals to form very regular LIPSS for replication processes, which allow the exact transfer of the structures from metallic materials to a broad palette of polymers (Figure 23) [100]. Using an elastomer, the fabrication of flexible surfaces with reversibly switchable optical response was demonstrated [100]. In particular, a linear elastic strain leads to a linear increase of the structural colour wavelengths emitted from the polymer surface, i.e. to a red-shift of the structural colours from blue to red in the visible electromagnetic spectrum (see lower part of Figure 24).

With regard to other surface properties, the advantages of replica casting compared to the direct production of large-area LIPSS on polymers are given by its high reproducibility without laser-induced modifications of the material structure and surface chemistry (see Ch. 2). Moreover, replica casting provides the possibility to scale to structuring process to surface areas in the range of μm^2 to m^2. Refractive beam shaping can then be used to control the LIPSS formation within the focal spot, which is of interest for the fabrication of novel, bioinspired complex surface structures [48].

3.2 Wetting of surfaces

Aside from the optical properties, controlling the wettability with liquid water and other liquids as well as superhydrophobic properties is probably one of the most studied examples of studies on LIPSS-based surfaces. The modification of surface wetting was studied mainly on

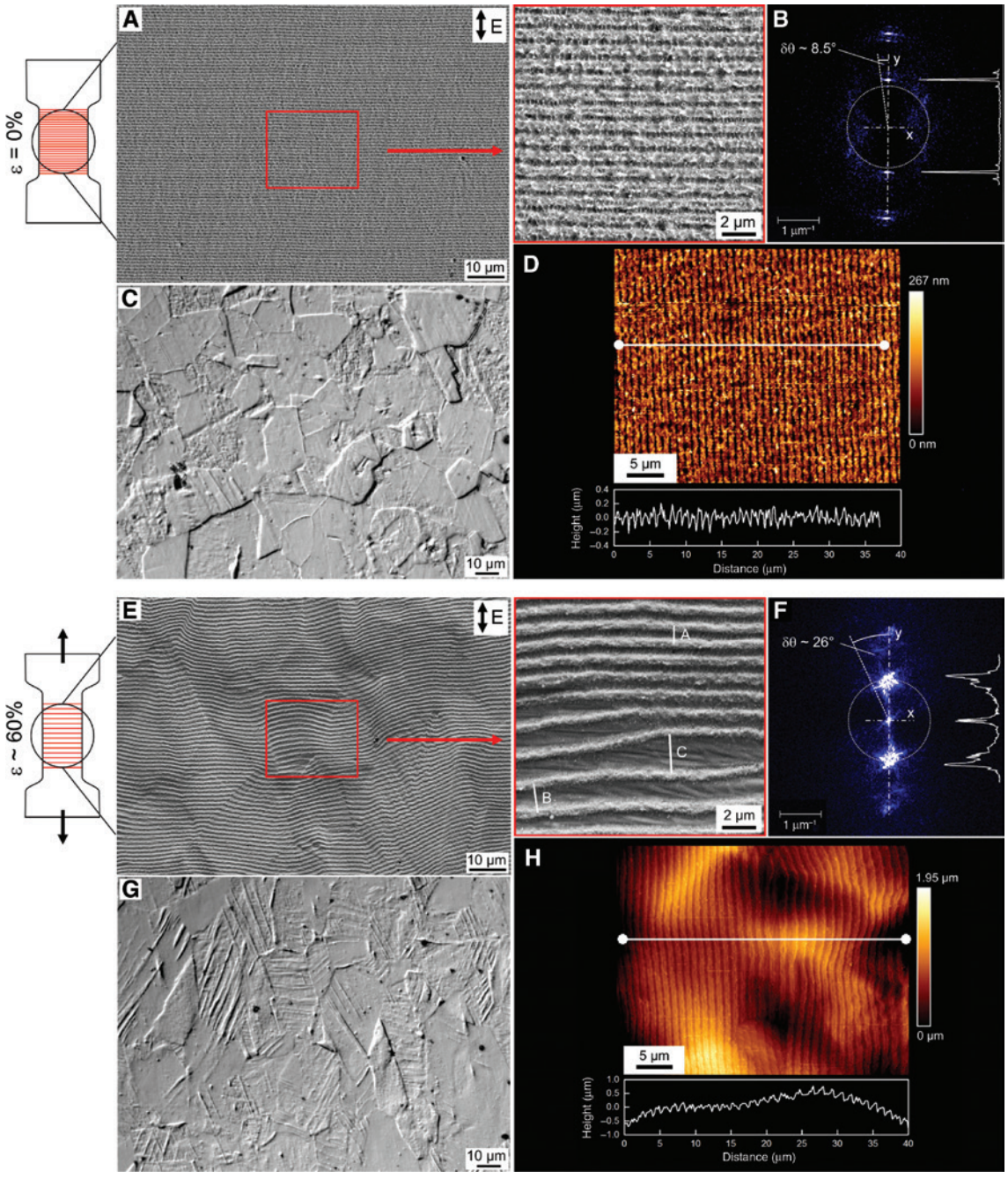

Figure 22: Surface morphology of stainless steel X2CrNiMo17-12-2 depending on its plastic deformation: (A–D) Refer to the material surface before plastic deformation showing (A) SEM micrographs of LIPSS fabricated by fs-laser irradiation with $F = 1\,\mathrm{J/cm^2}$, (B) Fourier transform of the LIPSS, (C) optical micrograph of the microstructure of the non-irradiated material and d) AFM micrographs of the surface topography. (E–H) the material surface after plastic deformation (total strain $\varepsilon = \sim 60\%$) showing (E) SEM micrographs of the LIPSS, (F) the Fourier transform of the modified LIPSS, (G) the microstructure of the deformed material without LIPSS and (H) AFM micrographs of the surface topography. In the Fourier transform, $\delta\theta$ represents the dispersion of the LIPSS orientation angle, the utilised laser wavelength $\lambda = 1025$ nm is represented by the dotted circle, and the insets illustrate the cross sections of Fourier spectra. Note the different scaling of the height axis in the AFM micrographs. Reprinted from [100], with permission from Elsevier.

metals, particularly concerning the transition of hydrophilic to hydrophobic metal surfaces [38, 42], but also on fused silica [98] and silicon [8, 40]. The manufacturing of superhydrophobic surfaces is generally divided into the following two strategies. The first approach focuses on increasing the surface roughness of a raw material with low

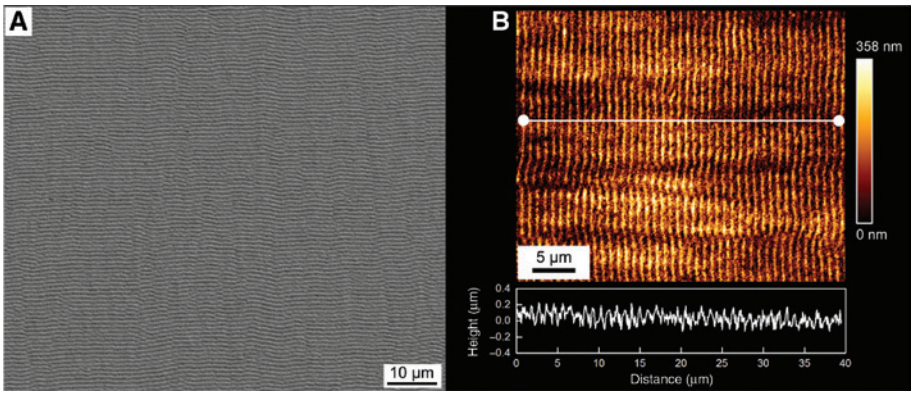

Figure 23: The (A) SEM and (B) AFM micrographs of LIPSS fabricated on polyvinyl siloxane by replica casting using a stainless steel master. Reprinted from [100], with permission from Elsevier.

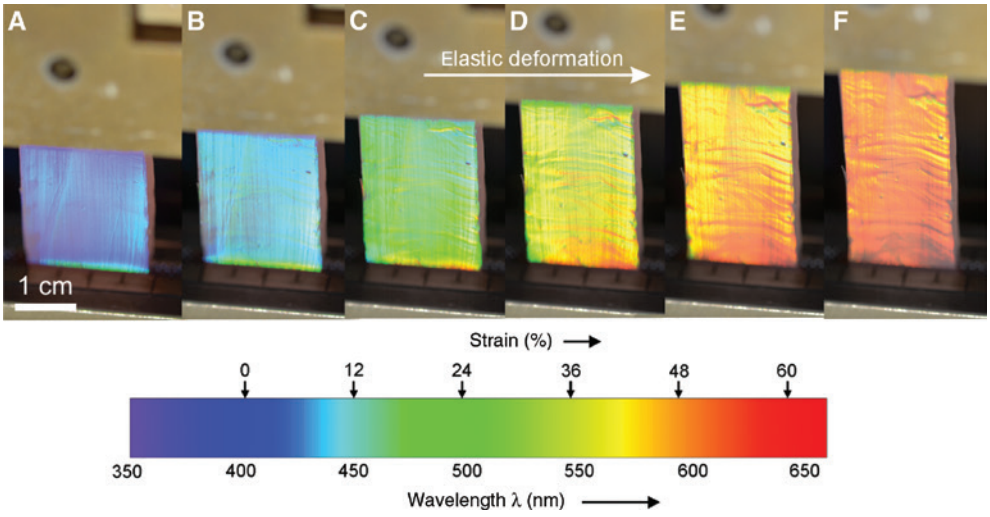

Figure 24: The structural colours resulting from LIPSS fabricated by replica casting using a stainless steel master: Elastic deformation with a total strain of (A) $\varepsilon = 0\%$, (B) $\varepsilon = 12\%$, (C) $\varepsilon = 24\%$, (D) $\varepsilon = 36\%$, (E) $\varepsilon = 48\%$ and (F) $\varepsilon = 60\%$ results in a reversible mechano-responsive colour-change in the visible electromagnetic spectrum from blue to red. Reprinted from [100], with permission from Elsevier.

surface energy [102]. The second concept involves increasing the surface roughness to achieve a hydrophilic intermediate state in combination with a post-chemical surface functionalisation (e.g. coatings, silanisation or additional treatments) to obtain the final hydrophobic wettability behaviour [98]. The impact of hierarchical surface topographies of ordered microstructures superimposed with LIPSS on wetting was also studied by several groups [98, 103]. Using stainless steel as an example, it was shown that hierarchical structures enable hydrophobic surfaces prepared from the initially hydrophilic surface without additional functionalization [103]. Investigations on the wettability of LIPSS-based surfaces revealed a time-dependent change in contact angle for various metals [38]. The aging effect emphasises the strong impact of the surface chemistry in the context of wetting and leads to a change of the contact angle from hydrophilic immediately after laser structuring to hydrophobic with increasing time (several days to weeks) [38, 42]. For non-metallic materials, such as Si, the hydrophilic surface state after fs-laser irradiation was determined to be stable over time [40].

Composite surfaces allow the investigation of various aspects concerning homogenous and heterogeneous wetting with different liquids [6–8]. For the metal-semiconductor composite (Ag-Si), the static surface contact angle with distilled water was analysed before and after fs-laser irradiation with $F = 0.3$ J/cm² (Figure 25A) [8]. For this purpose, the sessile drop method was used [104]. This method, well-established for the characterisation of surface wetting, is based on an optical evaluation of a drop applied to a materials surface, i.e. the contact angle is determined from a profile or side view image taken by a high-resolution

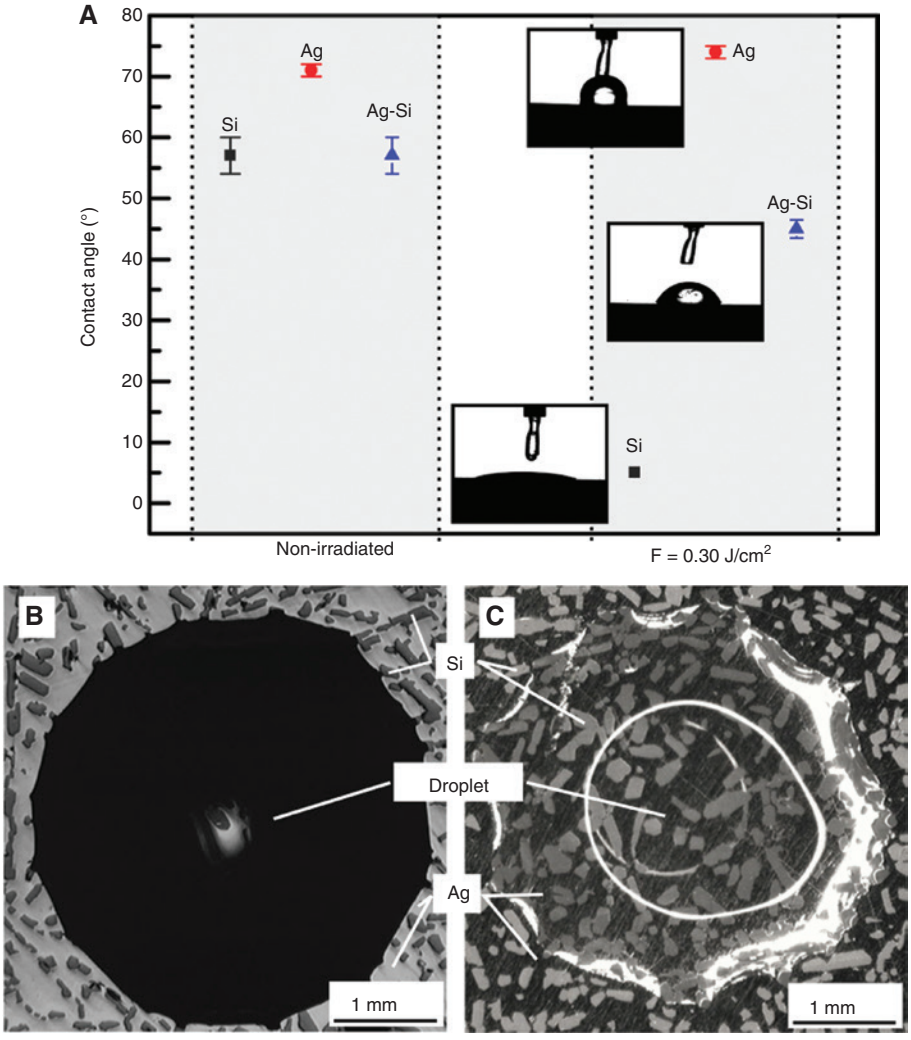

Figure 25: Global wettability analysis before and after fs-laser irradiation with $F = 0.30$ J/cm² and $N = 18$: (A) Contact angles of distilled water on the Si, Ag and Ag-Si composite surfaces. The insets show the corresponding side view images of the droplet after fs-laser irradiation. (B, C) Optical microscopy top views of the Ag-Si composite surface with a distilled water droplet before and after fs-laser irradiation, respectively. Reprinted with permission from [8]. Copyright (2019) American Chemical Society.

camera. Before fs-laser irradiation, the contact angles of both the individual Ag and Si components, measured as reference, and the composite ranged from 55°–71°, indicating that the surfaces are slightly hydrophilic.

Despite the fs-laser irradiation, the contact angle of the polished Ag surface remains almost unaffected, as the selected fs-laser peak fluence was below the LIPSS formation threshold of Ag. On the Si surface, however, the LIPSS structuring results in a strongly wetting surface characterised by a very small contact angle of about 5°. In line with the metal-ceramic-matrix composites, this transition is caused by the increased surface roughness [102]. The behaviour of the single components finally leads to a decrease of the global contact angle of the composite, which means that the entire composite surface becomes more hydrophilic (Figure 25A).

As already mentioned in Ch. 2, the very large decrease of the contact angle on pure Si cannot be attributed solely to a laser-induced increase in roughness. In addition to the topographical aspects, the wetting is strongly influenced by the laser-induced oxidation of the Si surface during LIPSS formation [8, 40]. Furthermore, the contact angle measured for the selectively structured composite also deviates from theoretical predictions [102, 105]. This results from the large difference of the contact angle between the irradiated Si crystallites and the surrounding Ag matrix ($\Delta\theta = \sim 69°$). As a consequence, the wetting conditions vary locally and therefore the shape of the applied droplet changes significantly when compared to the non-irradiated surface (Figure 25B, C). The enlarged views in Figure 26A and B

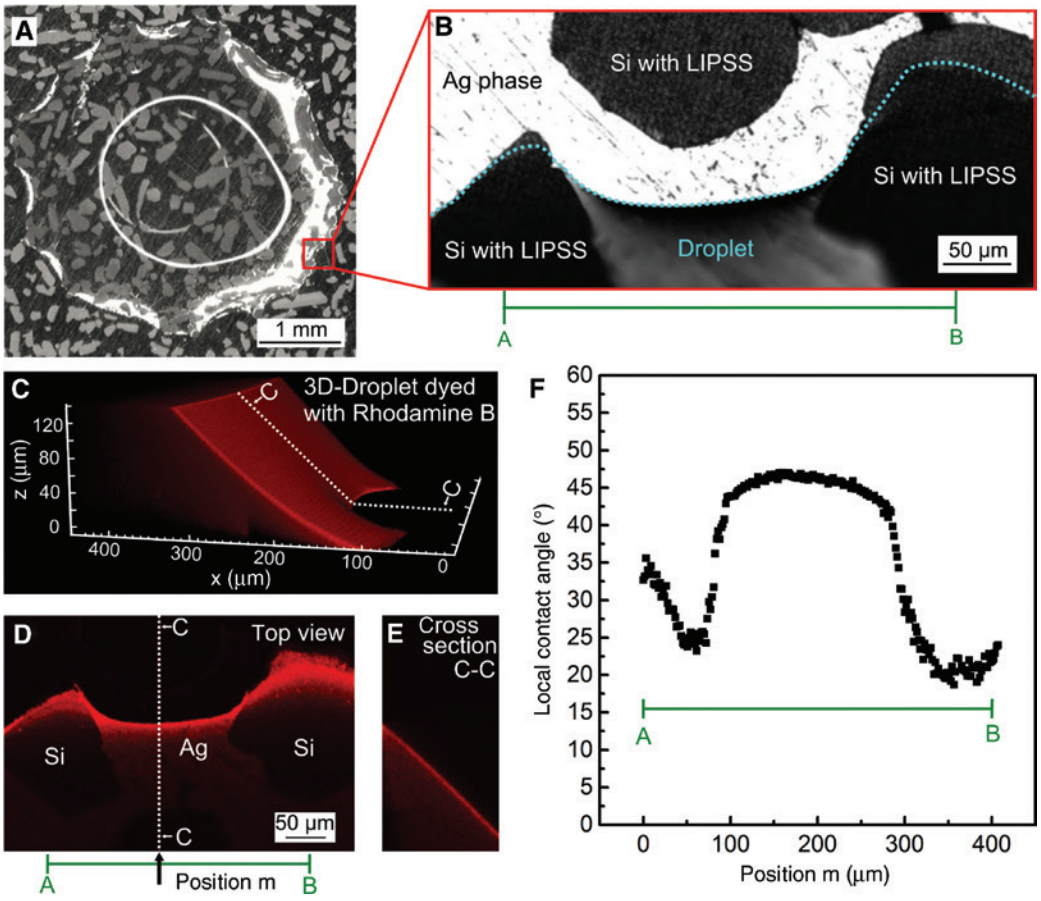

Figure 26: The local wettability analysis of the Ag-Si composite after fs-laser irradiation with $F = 0.30$ J/cm² and $N = 18$: (A, B) Top view OM image of a droplet on the Ag-Si surface. (C) 3D-model of the edge of a droplet dyed with Rhodamine B as acquired by CLSM. (D) Corresponding top view of the captured droplet over CLSM and (E) exemplary part of the cross section (C-C) of the droplet model parallel to the z-x-plane utilised for local contact angle measurement. Position of the cross section is indicated by the white dashed line in (C). (F) Local contact angle as function of the vertical position along the green line A to B (as displayed in (B, D)). Reprinted with permission from [8]. Copyright (2019) American Chemical Society.

illustrate how the droplet contour is displaced according to the phases involved at the surface. However, this effect is not captured by the perspective of the established sessile drop method.

A suitable approach to quantify this strongly heterogeneous wetting behaviour of the composite is based on the determination of the local contact angle on the surface [106]. For this purpose, the droplet was dyed with the fluorescence agent Rhodamine B, aftet which a 3D model of the droplet was generated by *z*-stacking the droplet on the Ag-Si composite surface by means of CLSM [8]. The corresponding software provides different perspectives of the droplet, such as a 3D view (Figure 26C), the top view (Figure 26D) and cross-sections of the droplet (Figure 26E). The cross-sections are used to determine the local contact angle on the surface at specific positions m along the boundary of the droplet (Figure 26F). The corresponding results demonstrate the wide change of the contact angle ranging from 20° to about 45° depending on the position at the composite surface.

Based on the displacement of the droplet contour from the Ag phase in the direction of the strongly hydrophilic Si crystallites, a targeted or directed droplet movement was studied as a potential application of heterogeneous wetting [8]. Alternative approaches to realise directional liquid motion are based on the bioinspired surface structures with specific geometries or with gradients in the structural sizes [86, 107]. The Ag-Si composite was investigated using a macroscopic interface selectively structured with LIPSS using a contact angle measurement device equipped with a high-speed camera (Figure 27A). The resulting photographs demonstrate that a droplet applied on the weakly hydrophilic Ag phase is attracted by the nanostructured, strongly hydrophilic Si surface and distributed within a very short time scale (about 83 ms) over the entire silicon phase (Figure 27).

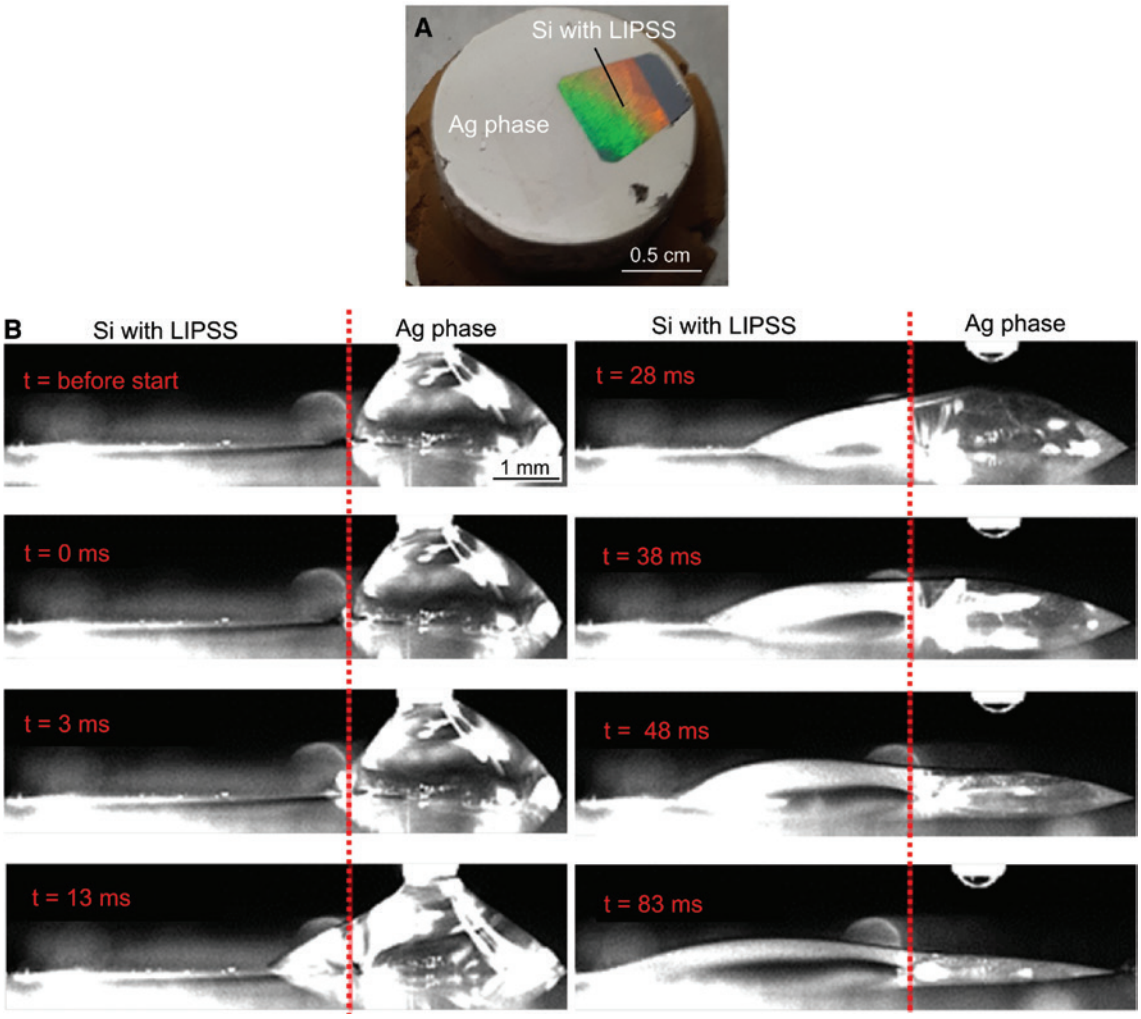

Figure 27: The droplet motion at a macroscopic Ag-Si boundary: (A) Photograph of the macroscopic Ag-Si boundary, where the Si phase is covered with LIPSS and (B) Droplet movement at the Ag-Si boundary (red dotted line) captured by high-speed camera at different times. Reprinted with permission from [8]. Copyright (2019) American Chemical Society.

3.3 Tribological properties

Surface engineering in terms of tribological properties strongly depends on surface roughness that determines the contact area and stress and provides lubricant paths and reservoirs. LIPSS-based micro- and nanostructures aimed at improving the tribological performance of surfaces were first proposed in 1999 by Yu and Lu [108]. Since then, the impact of LIPSS on friction and wear were investigated amongst others on metals [39, 109, 110], carbon materials [111, 112], ceramics [112] and composite materials [7]. The corresponding literature highlights LIPSS as a promising approach to reduce the friction coefficient and wear. The advantages compared to conventional methods are the relatively simple manufacturability of LIPSS and the possibility of their selective generation. General statements, however, are difficult to make due to the sometimes very different tribological testing conditions. These include, in particular, the different material pairings, testing with or without lubricants, type of lubricant used, loads, contact geometries, velocities and varying geometric parameters of the generated LIPSS [113]. Especially with regard to lubricants, studies reported that the chemical composition (e.g. additives in engine oil) significantly influences the reduction of friction and wear for sliding of different metals [39, 109].

Comparative studies between HSFL and LSFL on titanium revealed that HSFL with a noticeably smaller period and depth have no significant influence on friction behaviour [110]. The destroyed surface after tribological analysis suggests that the LIPSS depth plays a very important role and that a positive friction behaviour requires surface

structures deeper than the sample deformation induced by the tribological tests [110]. Moreover, studies on metals revealed the importance of laser-induced oxidation layers [7, 113], which are suitable for reducing friction and wear, mainly due to a modification of hardness or surface chemistry [113–116]. This aspect was also observed during the characterisation of the tribological performance of metal-ceramic composites (Al_2O_3-nZrO_2-Nb) using a reciprocating sliding tribological test in a ball-on-disc configuration with a 10 mm alumina ball as the counter body

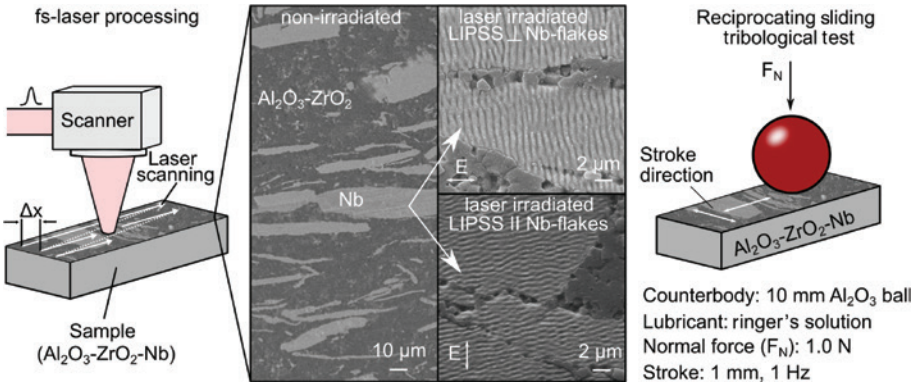

Figure 28: The schematic illustration of LIPSS formation and the tribological tests, including the investigated stroke directions parallel and perpendicular relative to the orientation of Nb-flakes and LIPSS, respectively.

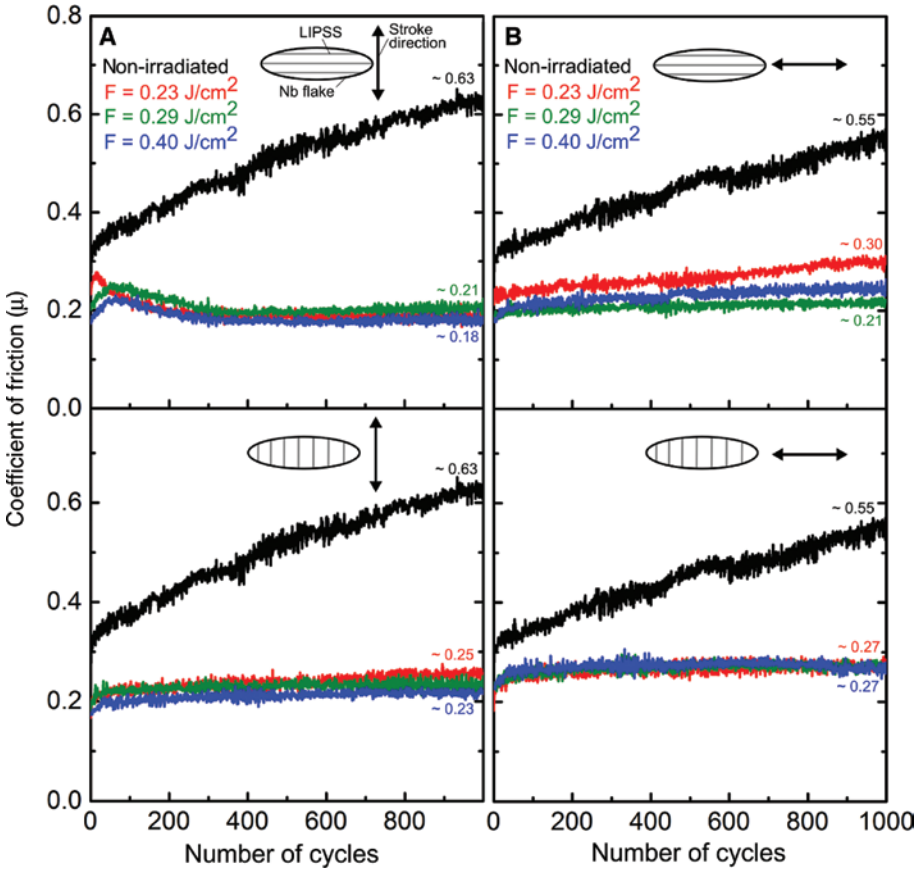

Figure 29: The friction coefficient μ as a function of the number of sliding cycles measured for the composite surfaces selectively structured with LIPSS using three different values of the fs-laser peak fluence *F* in comparison to the non-irradiated surface as reference. As indicated by the insets, the sliding direction was chosen (A) perpendicular and (B) parallel to the preferred orientation of the Nb-flakes. In both cases, the LIPSS orientation was additionally changed relative to the sliding direction. Reprinted from [7], with permission from Elsevier.

(Figure 28) [7]. For this purpose, the selectively structured composite surfaces were analysed at a normal force of 1 N for a total number of 1000 cycles using Ringer's solution as lubricant. The Ringer's solution aimed on simulating physiological conditions in view of the potential use of the composite as an implant material. The results were compared to non-irradiated surfaces as reference. The studies focussed on directional dependencies with respect to flake alignment and LIPSS orientation. For this purpose, the nanostructures were produced parallel and perpendicular to the preferred orientation of the flakes by means of the linear beam polarisation. The tribological tests were then performed in both directions parallel and perpendicular to the Nb-flakes.

Figure 29 shows the resulting friction coefficient μ measured for different values of the fs-laser peak fluence F and stroke directions as a function of the number of measurement cycles. As a main finding for the non-irradiated surface, the representing black curves show a remarkable increase of μ with increasing number of cycles starting from the initial value of about 0.3 in each case to values ranging from 0.55 to 0.63. Thus, the friction coefficient of the non-irradiated surface increases by a factor of about 2 during the measurement. After fs-laser irradiation, the selective LIPSS formation results in smaller initial values of about 0.2. These values remain almost constant during the chosen number of measurement cycles, thus leading to a reduction of the friction coefficient by a factor of about 3. However, considering the experimental uncertainty of the measurements, a significant influence of the orientation of Nb-flakes and LIPSS was not observed [7].

The analysis of the non-irradiated surface without LIPSS after tribological testing indicates a clearly visible wear track, which is confirmed in the corresponding SEM micrograph by abrasion and some cracks that can be detected at the surface (Figure 30A and B). On the contrary, the wear tracks on the surfaces structured with LIPSS parallel (Figure 30C and D) and perpendicular (Figure 30E and F) to the Nb-flakes are difficult to observe. Only some bright spots in the optical micrographs indicate wear. The SEM micrographs rather demonstrate that the LIPSS can still be observed in both directions after tribological testing, thus confirming an increased wear resistance in line with the much lower friction coefficient measured for the structured surfaces. Similar results were reported by Bonse et al. for the friction analysis of titanium structured

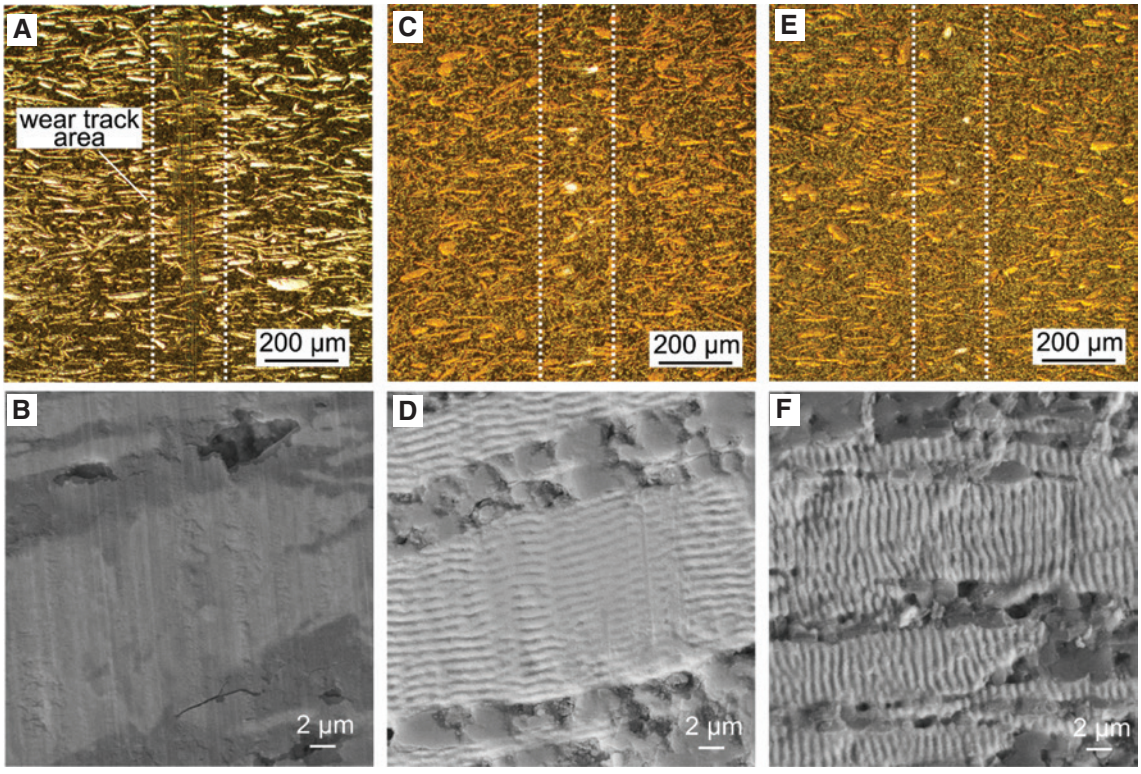

Figure 30: The optical and SEM micrographs obtained from the composite surface showing wear tracks after tribological testing: (A, B) non-irradiated surface, (C, D) surface structured with LIPSS ($F = 0.40$ J/cm^2) parallel to Nb-flakes and (E, F) surface structured with LIPSS ($F = 0.40$ J/cm^2) perpendicular to Nb-flakes. In all micrographs, the sliding direction was chosen perpendicular to the Nb-flakes. Reprinted from [7], with permission from Elsevier.

with LIPSS [39, 113]. The EDX analyses of the wear tracks on the composite surfaces with regard to the main elements Al, O, and Nb confirm the more intensive abrasion on the non-irradiated surface by a blurring of the boundaries and of the elemental distribution in the created EDX maps [7]. Consequently, Al from both the matrix and the alumina ball can be found on the Nb-flakes after tribological testing and Nb from the flakes is deposited on the matrix. Moreover, the much sharper element distribution after LIPSS formation clearly indicates a less intensive abrasion. The small amount of Nb result from the ablation process due to LIPSS formation.

The improved tribological behaviour was discussed by a combination of several influencing factors. Wetting analyses with distilled water and Ringer's solution revealed a more hydrophilic surface caused by LIPSS formation, which leads to an effective distribution of the lubricant. This behaviour was discussed under consideration of the increased surface roughness on the Nb-flakes resulting from LIPSS formation based on the well-accepted models of Cassie [105] and Wenzel [102]. However, these models only consider the topographical aspects. The chemical surface composition plays a key role for both wettability and the tribological properties [38, 113], and this also includes the detected laser-induced oxidation layer on the Nb-flakes (Figure 19). In this context, a key aspect is related to the size of the contact area with respect to the size of the Nb-flakes and LIPSS. Moreover, the deformation of the surface in relation to its initial topography plays a very important role [7, 110]. Calculations based on the Hertzian elastic deformation model [117], under consideration of the testing conditions and material parameters, showed that the diameter of the contact areas is larger than the size of the individual Nb-flakes, which explains the minor influence of the orientation of flakes and LIPSS. Furthermore, the calculations propose a contact between LIPSS and the alumina ball during tribological testing, which is also experimentally proven by the slight wear of the LIPSS and abrasion marks in the SEM micrographs (Figure 30D and F).

4 Future perspectives

Studies on the fs-laser irradiation of different types of substrates with different material properties using well-defined processing parameters have proven the versatility of LIPSS-based surface nanostructuring. It offers a flexible tool for the LIPSS-based fabrication of functional surfaces. This potential was discussed, amongst other things, using the example of mechano-responsive changes in structural colours, homogeneous and heterogeneous wetting of substrate surfaces and the tribological properties of composite materials selectively structured with LIPSS. The mechano-responsive colour-change of LIPSS on metals and polymers is of particular interest for the development of novel switches and safety devices. The demonstrated adjustable wetting behaviour and alignment of LIPSS might be of potential interest for biomedical applications, including the control of cell adhesion, proliferation and differentiation [53, 118] as well as for the creation of antibacterial surfaces [119]. Moreover, surfaces with heterogeneous wetting properties might be suitable for various applications in microfluidics [107, 120]. From a fundamental point of view, further investigation of composites will expand the existing knowledge on the formation process of LIPSS. This concerns, in particular, the electromagnetic interaction of the fs-laser radiation with the material at the interface between the composite components, as materials with very different electrical and optical properties can be combined.

References

[1] J. Bonse, S. Höhm, S. V. Kirner, A. Rosenfeld and J. Krüger, IEEE J. Select. Top. Quant. Electron. 23, 9000615 (2017).
[2] F. A. Müller, C. Kunz and S. Gräf, Materials 9, 476 (2016).
[3] J. Bonse, S. V. Kirner, S. Höhm, N. Epperlein, D. Spaltmann, et al., Proc. SPIE 10092, 100920N (2017).
[4] A. Y. Vorobyev and C. Guo, Laser Photon. Rev. 7, 385–407 (2013).
[5] J. Bonse, J. Krüger, S. Höhm and A. Rosenfeld, J. Laser. Appl. 24, 042006 (2012).
[6] C. Kunz, J. F. Bartolomé, E. Gnecco, F. A. Müller and S. Gräf, Appl. Surf. Sci. 434, 582–587 (2018).
[7] C. Kunz, J. Bonse, D. Spaltmann, C. Neumann, A. Turchanin, et al., Appl. Surf. Sci. 499, 143917 (2019).
[8] F. R. Weber, C. Kunz, S. Gräf, M. Rettenmayr and F. A. Müller, Langmuir 35, 14990–14998 (2019).
[9] S. Gräf, C. Kunz, S. Engel, T. J. Y. Derrien and F. A. Müller, Materials 11, 1340 (2018).
[10] S. Gräf, C. Kunz and F. A. Müller, Materials 10, 933 (2017).
[11] E. Rebollar, J. R. V. de Aldana, I. Martin-Fabiani, M. Hernandez, D. R. Rueda, et al., Phys. Chem. Chem. Phys. 15, 11287–11298 (2013).
[12] D. C. Emmony, R. P. Howson and L. J. Willis, Appl. Phys. Lett. 23, 598–600 (1973).
[13] Z. Guosheng, P. M. Fauchet and A. E. Siegman, Phys. Rev. B 26, 5366–5381 (1982).
[14] J. E. Sipe, J. F. Young, J. S. Preston and H. M. van Driel, Phys. Rev. B 27, 1141–1154 (1983).
[15] J. F. Young, J. S. Preston, H. M. van Driel and J. E. Sipe, Phys. Rev. B 27, 1155–1172 (1983).
[16] J. F. Young, J. E. Sipe and H. M. van Driel, Phys. Rev. B 30, 2001–2015 (1984).

[17] F. Keilmann and Y. H. Bai, Appl. Phys. A Mater. Sci. Process. 29, 9–18 (1982).
[18] F. Garrelie, J. P. Colombier, F. Pigeon, S. Tonchev, N. Faure, et al., Opt. Express 19, 9035–9043 (2011).
[19] B. Rethfeld, D. S. Ivanov, M. E. Garcia and S. I. Anisimov, J. Phys. D: Appl. Phys. 50, 193001 (2017).
[20] J. Bonse, A. Rosenfeld and J. Krüger, J. Appl. Phys. 106, 104910 (2009).
[21] D. Dufft, A. Rosenfeld, S. K. Das, R. Grunwald and J. Bonse, J. Appl. Phys. 105, 034908 (2009).
[22] J. Bonse, M. Munz and H. Sturm, J. Appl. Phys. 97, 013538 (2005).
[23] G. D. Tsibidis, M. Barberoglou, P. A. Loukakos, E. Stratakis and C. Fotakis, Phys. Rev. B 86, 115316 (2012).
[24] J. P. Colombier, F. Garrelie, P. Brunet, A. Bruyere, F. Pigeon, et al., J. Laser. Micro Nanoen. 7, 362–368 (2012).
[25] E. L. Gurevich, Y. Levy, S. V. Gurevich and N. M. Bulgakova, Phys. Rev. B 95, 054305 (2017).
[26] E. L. Gurevich, Appl. Surf. Sci. 374, 56–60 (2016).
[27] E. L. Gurevich, Phys. Rev. E 83, 031604 (2011).
[28] E. B. Levchenko and A. L. Chernyakov, J. Exp. Theor. Phys. 81, 202–209 (1981).
[29] J. Reif, O. Varlamova, S. Varlamov and M. Bestehorn, Appl. Phys. A Mater. Sci. Process. 104, 969–973 (2011).
[30] O. Varlamova, F. Costache, J. Reif and M. Bestehorn, Appl. Surf. Sci. 252, 4702–4706 (2006).
[31] Q. H. Wu, Y. R. Ma, R. C. Fang, Y. Liao, Q. X. Yu, et al., Appl. Phys. Lett. 82, 1703–1705 (2003).
[32] J. Bonse, S. Höhm, A. Rosenfeld and J. Krüger, Appl. Phys. A Mater. Sci. Process. 110, 547–551 (2013).
[33] X. F. Li, C. Y. Zhang, H. Li, Q. F. Dai, S. Lan, et al., Opt. Express 22, 28086–28099 (2014).
[34] A. Borowiec and H. K. Haugen, Appl. Phys. Lett. 82, 4462–4464 (2003).
[35] R. Buividas, L. Rosa, R. Sliupas, T. Kudrius, G. Slekys, et al., Nanotechnol. 22, 055304 (2011).
[36] M. Straub, M. Afshar, D. Feili, H. Seidel and K. König, J. Appl. Phys. 111, 124315 (2012).
[37] A. Rudenko, J. P. Colombier, S. Höhm, A. Rosenfeld, J. Krüger, et al., Sci. Rep. 7, 12306 (2017).
[38] A. M. Kietzig, S. G. Hatzikiriakos and P. Englezos, Langmuir 25, 4821–4827 (2009).
[39] J. Bonse, R. Koter, M. Hartelt, D. Spaltmann, S. Pentzien, et al., Appl. Phys. A Mater. Sci. Process. 117, 103–110 (2014).
[40] O. Varlamova, J. Reif, M. Stolz, R. Borcia, I. D. Borcia, et al., Eur. Phys. J. B 92, 91 (2019).
[41] C. Kunz, T. N. Büttner, B. Naumann, A. V. Boehm, E. Gnecco, et al., Carbon 133, 176–185 (2018).
[42] P. Bizi-bandoki, S. Valette, E. Audouard and S. Benayoun, Appl. Surf. Sci. 273, 399–407 (2013).
[43] C. Florian, J.-L. Déziel, S. V. Kirner, J. Siegel and J. Bonse, Nanomaterials 10, 147 (2020).
[44] I. Gnilitskyi, T. J. Y. Derrien, Y. Levy, N. M. Bulgakova, T. Mocek, et al., Sci. Rep. 7, 8485 (2017).
[45] S. Gräf and F. A. Müller, Appl. Surf. Sci. 331, 150–155 (2015).
[46] A. Möhl, S. Kaldun, C. Kunz, F. A. Müller, U. Fuchs, et al., J. Laser. Appl. 31, 042019 (2020).
[47] O. J. Allegre, W. Perrie, S. P. Edwardson, G. Dearden and K. G. Watkins, J. Opt. 14, 085601 (2012).
[48] E. Skoulas, A. Manousaki, C. Fotakis and E. Stratakis, Sci. Rep. 7, 45114 (2017).
[49] J. Ouyang, W. Perrie, O. J. Allegre, T. Heil, Y. Jin, et al., Opt. Express 23, 12562–12572 (2015).
[50] J. J. J. Nivas, S. T. He, A. Rubano, A. Vecchione, D. Paparo, et al., Sci. Rep. 5, 17929 (2015).
[51] B. Dusser, Z. Sagan, H. Soder, N. Faure, J. P. Colombier, et al., Opt. Express 18, 2913–2924 (2010).
[52] B. Wu, M. Zhou, J. Li, X. Ye, G. Li, et al., Sci. Rep. 6, 36296 (2016).
[53] M. Martinez-Calderon, M. Manso-Silvan, A. Rodriguez, M. Gomez-Aranzadi, J. P. Garcia-Ruiz, et al., ACS Nano 3, 4062–4070 (2009).
[54] M. Huang, F. L. Zhao, Y. Cheng, N. S. Xu and Z. Z. Xu, ACS Nano 3, 4062–4070 (2009).
[55] A. J. Smith, C. Wang, D. Guo, C. Sun and J. Huang, Nat. Commun. 5, 5517 (2014).
[56] T. Jwad, P. Penchev, V. Nasrollahi and S. Dimov, Appl. Surf. Sci. 453, 449–456 (2018).
[57] A. H. A. Lutey, L. Gemini, L. Romoli, G. Lazzini, F. Fuso, et al., Sci. Rep. 8, 10112 (2018).
[58] U. Hermens, M. Pothen, K. Winands, K. Arntz and F. Klocke, Opt. Las. Engin. 101, 44–50 (2018).
[59] S. Schwarz, S. Rung, C. Esen and R. Hellmann, J. Laser. Micro Nanoen. 13, 90–94 (2018).
[60] L. Wang, Q. D. Chen, X. W. Cao, R. Buividas, X. W. Wang, et al., Light-Sci. Appl. 6, e17112 (2017).
[61] B. Stępak, P. Dzienny, V. Franke, P. Kunicki, T. Gotszalk, et al., Appl. Surf. Sci. 436, 682–689 (2018).
[62] E. V. Golosov, A. A. Ionin, Y. R. Kolobov, S. I. Kudryashov, A. E. Ligachev, et al., Phys. Rev. B 83, 115426 (2011).
[63] P. Feng, N. Zhang, H. Wu and X. Zhu, Opt. Lett. 40, 17–20 (2015).
[64] M. Huang, F. L. Zhao, Y. Cheng, N. S. Xu and Z. Z. Xu, Opt. Express 16, 19354–19365 (2008).
[65] R. Sajzew, J. Schröder, C. Kunz, S. Engel, F. A. Müller, et al., Opt. Lett. 40, 5734–5737 (2015).
[66] M. Huang, F. Zhao, Y. Cheng, N. Xu and Z. Xu, Opt. Express 16, 19354–19365 (2008).
[67] C. Freitag, R. Weber and T. Graf, Opt. Express 22, 1474–1479 (2014).
[68] A. C. Ferrari and D. M. Basko, Nat. Nanotechnol. 8, 235–246 (2013).
[69] J. Bonse, A. Hertwig, R. Koter, M. Weise, U. Beck, et al., Appl. Phys. A Mater. Sci. Process. 112, 9–14 (2013).
[70] P. Calvani, A. Bellucci, M. Girolami, S. Orlando, V. Valentini, et al., Appl. Phys. A Mater. Sci. Process. 117, 25–29 (2014).
[71] S. Höhm, A. Rosenfeld, J. Krüger and J. Bonse, J. Appl. Phys. 112, 014901 (2012).
[72] M. Grehn, T. Seuthe, M. Hofner, N. Griga, C. Theiss, et al., Opt. Mater. Express 4, 689–700 (2014).
[73] K. H. Sun, J. Am. Ceram. Soc. 30, 277–281 (1947).
[74] K. H. Sun and M. L. Huggins, J. Phys. Colloid Chem. 51, 438–443 (1947).
[75] V. V. Temnov, Ultrafast laser-induced phenomena in solids studied by time-resolved interferometry. PhD thesis, University of Duisburg-Essen, 2004.
[76] A. Ben-Yakar, A. Harkin, J. Ashmore, R. L. Byer and H. A. Stone, J. Phys. D: Appl. Phys. 40, 1447–1459 (2007).
[77] W. Martienssen and H. Warlimont, in 'Springer Handbook of Condensed Matter and Materials Data' (Springer, Heidelberg, New York, 2005).
[78] S. Gräf, G. Staupendahl, P. Gerling and F. A. Müller, J. Appl. Phys. 113, 013101 (2013).

[79] J. H. Wray and J. T. Neu, J. Opt. Soc. Am. 59, 774–776 (1969).
[80] A. Ben-Yakar, R. L. Byer, A. Harkin, J. Ashmore, H. A. Stone, et al., Appl. Phys. Lett. 83, 3030–3032 (2003).
[81] J. F. Bartolome, C. F. Gutierrez-Gonzalez and R. Torrecillas, Compos. Sci. Technol. 68, 1392–1398 (2008).
[82] C. F. Gutierrez-Gonzalez and J. F. Bartolomé, Wear 303, 211–215 (2013).
[83] C. F. Gutierrez-Gonzalez and J. F. Bartolomé, J. Mater. Res. 23, 570–578 (2008).
[84] T. J. Y. Derrien, R. Koter, J. Krüger, S. Höhm, A. Rosenfeld, et al., J. Appl. Phys. 116, 074902 (2014).
[85] S. T. Wang, K. S. Liu, X. Yao and L. Jiang, Chem. Rev. 115, 8230–8293 (2015).
[86] U. Hermens, S. V. Kirner, C. Emonts, P. Comanns, E. Skoulas, et al., Appl. Surf. Sci. 418, 499–507 (2017).
[87] G. Q. Li, J. W. Li, Y. L. Hu, C. C. Zhang, X. H. Li, et al., Appl. Phys. A Mater. Sci. Process. 118, 1189–1196 (2015).
[88] A. Y. Vorobyev and C. Guo, Appl. Phys. Lett. 92, 041914 (2008).
[89] M. S. Ahsan, F. Ahmed, Y. G. Kim, M. S. Lee and M. B. G. Jun, Appl. Surf. Sci. 257, 7771–7777 (2011).
[90] Z. G. Ou, M. Huang and F. L. Zhao, Opt. Express 22, 17254–17265 (2014).
[91] B. Dusser, E. Audouard, M. Jourlin, H. Soder and A. Foucou, "Method and device for marking a surface using controlled periodic nanostructures," Patent No. WO/2009/090324 (2007).
[92] Z. G. Ou, M. Huang and F. L. Zhao, Opt. Laser Technol. 79, 79–87 (2016).
[93] Y. Yang, J. J. Yang, C. Y. Liang and H. S. Wang, Opt. Express 16, 11259–11265 (2008).
[94] A. Papadopoulos, E. Skoulas, A. Mimidis, G. Perrakis, G. Kenanakis, et al., Adv. Mater. 31, 1901123 (2019).
[95] A. Y. Vorobyev and C. Guo, J. Appl. Phys. 103, 043513 (2008).
[96] A. Y. Vorobyev and C. Guo, Opt. Express 19, A1031–A1036 (2011).
[97] H. D. Yang, X. H. Li, G. Q. Li, C. Wen, R. Qiu, et al., Appl. Phys. A Mater. Sci. Process. 104, 749–753 (2011).
[98] C. Kunz, F. Müller and S. Gräf, Materials 11, 789 (2018).
[99] B. K. Nayak and M. C. Gupta, Opt. Las. Engin. 48, 940–949 (2010).
[100] S. Gräf, C. Kunz, A. Undisz, R. Wonneberger, M. Rettenmayr, et al., Appl. Surf. Sci. 471, 645–651 (2019).
[101] D. Yan, C. C. Tasan and D. Raabe, Acta Mater. 96, 399–409 (2015).
[102] R. N. Wenzel, Chem. Res. 28, 988–994 (1936).
[103] M. Martinez-Calderon, A. Rodriguez, A. Dias-Ponte, M. C. Morant-Minana, M. Gomez-Aranzadi, et al., Appl. Surf. Sci. 374, 81–89 (2016).
[104] D. Y. Kwok and A. W. Neumann, Adv. Colloid Interface Sci. 81, 167–249 (1999).
[105] A. B. D. Cassie, Discuss. Faraday Soc. 3, 11–16 (1948).
[106] J. Drelich, J. L. Wilbur, J. D. Miller and G. M. Whitesides, Langmuir 12, 1913–1922 (1996).
[107] S. V. Kirner, U. Hermens, A. Mimidis, E. Skoulas, C. Florian, et al., Appl. Phys. A – Mater. Sci. Process. 123, 754 (2017).
[108] J. J. Yu and Y. F. Lu, Appl. Surf. Sci. 148, 248–252 (1999).
[109] J. Bonse, R. Koter, M. Hartelt, D. Spaltmann, S. Pentzien, et al., Appl. Surf. Sci. 336, 21–27 (2015).
[110] J. Bonse, S. Höhm, R. Koter, M. Hartelt, D. Spaltmann, et al., Appl. Surf. Sci. 374, 190–196 (2015).
[111] N. Yasumaru, K. Miyazaki and J. Kiuchi, Appl. Surf. Sci. 254, 2364–2368 (2008).
[112] N. Yasumaru, K. Miyazaki, J. Kiuchi and E. Sentoku, Diamond Relat. Mater. 20, 542–545 (2011).
[113] J. Bonse, S. V. Kirner, M. Griepentrog, D. Spaltmann and J. Krüger, Materials 11, 801 (2018).
[114] S. V. Kirner, T. Wirth, H. Sturm, J. Krüger and J. Bonse, J. Appl. Phys. 122, 104901 (2017).
[115] S. V. Kirner, N. Slachciak, A. M. Elert, M. Griepentrog, D. Fischer, et al., Appl. Phys. A Mater. Sci. Process. 124, 326 (2018).
[116] K. Aniolek, M. Kupka, A. Barylski and G. Dercz, Appl. Surf. Sci. 357, 1419–1426 (2015).
[117] H. Hertz, Journal für die reine und angwandte Mathematik 92, 156–171 (1881).
[118] T. J. Webster and E. S. Ahn, Tissue Engineering II: Basics of Tissue Engineering and Tissue Applications 103, 275–308 (2007).
[119] S. D. Puckett, E. Taylor, T. Raimondo and T. J. Webster, Biomaterials 31, 706–713 (2010).
[120] F. Mumm, A. T. J. van Helvoort and P. Sikorski, Acs Nano 3, 2647–2652 (2009).

Stephan Gräf
Otto Schott Institute of Materials Research (OSIM), Friedrich Schiller University Jena
Löbdergraben 32, 07743 Jena, Germany
stephan.graef@uni-jena.de
https://orcid.org/0000-0003-2849-1377

Stephan Gräf is a researcher and working group leader at the Otto Schott Institute for Materials Research at the Friedrich Schiller University in Jena. He received his PhD in 2010 from the Friedrich Schiller University Jena in the field of laser welding with dynamically polarised CO_2 laser radiation. Within the past years his work mainly focused on the engineering of material surfaces with tailored functional properties. This includes the detailed study of laser-matter interaction with regard to different wavelengths and pulse durations as well as laser-assisted micro- and nanostructuring of surfaces, particularly the fabrication of laser-induced periodic surface structures using ultrashort pulsed laser radiation.